



High-Performance Polyamide/Carbon Fiber Composites for Fused Filament Fabrication: Mechanical and Functional Performances

Sithiprumnea Dul, Luca Fambri, and Alessandro Pegoretti

Submitted: 17 December 2020 / Revised: 22 February 2021 / Accepted: 27 February 2021 / Published online: 19 April 2021

This study is focused on the 3D printing by fused filament fabrication (FFF) process of short carbon-fiber-reinforced polyamide (PA) composites. In particular, the effect of short carbon fiber (CF) on the mechanical, electrical and piezoresistivity properties of 3D-printed polyamide (PA) composite parts has been analyzed. In comparison with neat PA, the results revealed that the carbon fibers effectively improved all assessed mechanical properties of PA/CF composites. In particular, in XY build orientation, PA/CF 3D-printed composites exhibited a tensile strength of 96 MPa and a tensile modulus of 7.9 GPa, with an increment of + 34 and + 147%, respectively, when compared to the neat PA. Interlayer strength of 3D-printed PA and PA/CF composites reaches similar values, in the range 26–28 MPa. The impact strength of 3D-printed XY parts was reduced by the presence of CF. However, the fracture toughness of PA/CF composite 3D-printed parts was slightly higher in comparison with that of neat PA. Electrical resistivity of PA/CF 3D-printed parts is gradually decreasing from 1.7×10^4 to $0.7 \times 10^4 \Omega \text{ cm}$ in the temperature range from -16 to $100 \text{ }^\circ\text{C}$. The piezoresistivity tests revealed that an exponential resistance change occurs for both compression-molded and 3D-printed PA/CF samples once strained in tension. A gauge factor of 3D-printed parts of about 65 ± 5 was determined from cyclic strains in the elastic region.

Keywords additive manufacturing, carbon fiber-reinforced composites, high-temperature composites, mechanical properties, piezoresistivity, polyamide

1. Introduction

Additive manufacturing (AM), also known as 3D printing, is a technology to build objects layer by layer based on computer-aided design (CAD). In the fabrication process of a 3D object, successive layers are laid down starting from various forms of liquid, powder or sheet materials by using an AM machine. This technology has several benefits such as the possibility to fabricate a final part without using auxiliary tool/molds and offering solutions for the manufacturing of parts that are difficult to be produced by conventional methods. It also exhibits clear advantages over removal or subtractive manufacturing methodologies because no waste material is gener-

ated. Additive manufacturing is more suitable for customized products and prototypes, but also for relatively low-volume end-use productions.

According to ASTM Committee F42 (Ref 1) on additive manufacturing technologies, all additive manufacturing techniques can be classified into seven categories: materials extrusion, powder bed fusion, vat photopolymerization, binder jetting, materials jetting, sheet lamination and directed energy deposition. Fused filament fabrication (FFF) is a technique in the subgroup of materials extrusion, which is among the leading 3D-printing methods. In this process, a thermoplastic-based filament is extruded at a temperature above its glass transition (by about $100\text{--}150 \text{ }^\circ\text{C}$) or melting (by about $20\text{--}30 \text{ }^\circ\text{C}$) temperatures through a nozzle and deposited layer by layer on a platform to build a 3D object. The FFF process is characterized by various parameters which can influence the quality of the 3D-printed components such as build orientation, layer height, infill pattern and density, printing temperature (at nozzle, bed and printing environment) (Ref 2–4). Since 3D printing leads to non-isotropic parts, the build orientation is a critical parameter.

The mechanical and functional properties of thermoplastic composite materials can be targeted in view of specific applications. In general, fiber-reinforced (e.g., glass fiber, carbon fiber) composites have remarkable mechanical properties, leading to successful uses in various applications (Ref 5). In the meantime, 3D printing of fiber-reinforced composites is a new field in additive manufacturing. The mechanical properties of 3D-printed composite parts containing short fibers are inferior to those of continuous-fiber reinforced composites. However, 3D printing of short-fiber composites is more economical and feasible by direct printing with low-cost commercially available 3D printers. The use of fiber-reinforced composites and nanocomposites in 3D printing has been widely

This invited article is part of a special topical focus in the *Journal of Materials Engineering and Performance* on Additive Manufacturing. The issue was organized by Dr. William Frazier, Pilgrim Consulting, LLC; Mr. Rick Russell, NASA; Dr. Yan Lu, NIST; Dr. Brandon D. Ribic, America Makes; and Caroline Vail, NSWC Carderock.

Supplementary Information The online version contains supplementary material available at <https://doi.org/10.1007/s11665-021-05635-1>.

Sithiprumnea Dul, Luca Fambri, and Alessandro Pegoretti, Department of Industrial Engineering and INSTM Research Unit, University of Trento, Via Sommarive 9, 38123 Trento, Italy. Contact e-mail: alessandro.pegoretti@unitn.it.

investigated and reviewed in the recent literature (Ref 6-10). Various fiber-reinforced thermoplastic composites have been used for 3D printing with FFF. For instance, Reverte et al. (Ref 11) used a commercial polylactic acid (PLA)/CF filament for 3D printing. The strength and modulus of 3D-printed parts reached 70.3 MPa and 9.2 GPa, respectively. Tekinalp et al. (Ref 12) reported that 40 wt.% CF in acrylonitrile-butadiene-styrene (ABS) composites imparted strength and elastic modulus values of about 67 MPa and 13.8 GPa, with an increment of 115 and 700%, respectively, over the neat matrix. In composites, they also observed a high fiber orientation in the printing direction and decreased void content between beads. Spoerk et al. (Ref 13) also 3D-printed samples by using a commercial composite filament with 15 wt.% CF in polypropylene (PP). 3D-printed samples of PP/CF composite exhibited a tensile strength of 74.2 MPa and a modulus of 5.6 GPa. Wang et al. (Ref 14) used carbon fiber and glass fiber as reinforced fibers in polyether ether ketone (PEEK). PEEK/CF 5 wt.% and PEEK/GF 5 wt.% composites manifested strength values of 86.0 MPa and 94.0 MPa, respectively. Liao et al. (Ref 15) found that the tensile strength and modulus of polyamide12 (PA12) composites containing 10 wt.% of CF reached values of 94 MPa and 3.6 GPa, respectively. Lupone et al. (Ref 16) printed a commercial filament with a polyamide (PA) containing 15 wt.% of CF reaching values of 72.9 MPa and 7.73 GPa in tensile strength and modulus, respectively. Apart from mechanical reinforcement, CF in composites can be used also to achieve specific functionalities of components. Only a few papers are focused on the thermal (Ref 15, 17) and electrical (Ref 16) conductivity on 3D-printable CF composites. A study on the use of continuous fiber-reinforced composites for 3D printing of strain sensors by using copper and nichrome wires was performed. A linearity in the relative change in resistance with deformation was found with a gauge factor of 1.17 and 1.13 for the composites containing copper and nichrome, respectively (Ref 18).

In this study, commercially available polyamide and carbon fiber-reinforced PA composite (PA/CF) were extruded into filaments suitable for the FFF technique. Tensile, flexural, fracture toughness and impact tests of 3D-printed samples were performed for a full mechanical characterization. The effect of carbon fiber reinforcement in PA was compared between 3D-printed and compression-molded samples. The effects of two different build orientations in 3D printing (i.e., XY and Z) were also analyzed. Moreover, the electrical resistivity and strain monitoring of 3D-printed composites were also studied.

2. Materials and Methods

2.1 Materials

High-temperature polyamide (tradename LUVOCOM[®] 3F PA^{HT} 9825NT) and high-temperature polyamide with carbon fibers (tradename LUVOCOM[®] 3F PA^{HT} CF 9742BK) used in this study were kindly provided by Lehmann & Voss & Co KG (Hamburg, Germany). According to the producer's technical data sheet, LUVOCOM[®] 3F PA^{HT} CF 9742BK contains 15 wt.% of carbon fibers, while PA and PA/CF are characterized by a density of 1.20 g/cm³ and 1.25 g/cm³, respectively. Before processing, PA^{HT} and PA^{HT}-CF chips were dried under vacuum at 120 °C for 24 h with 0.3 wt.% and 1 wt.% of mass

loss, respectively. Thermogravimetric analysis in inert atmosphere, performed with a Mettler TG50 thermobalance, revealed a residue of about 9.9% and 26.7% for PA and PA/CF, respectively (Fig. S1).

2.2 Materials Processing and Sample Preparations

2.2.1 Compression Molding (CM). Dried pellets were compression molded using a Carver Laboratory press (Carver, Inc., Wabash, IN, USA) at 280 °C for 10 min under a load of 10 tons. Square plates (120 × 120 × 2 mm), (150 × 100 × 4 mm) and (100 × 100 × 5 mm) were produced. 1BA dumbbell samples were cut by using water jetting.

2.2.2 Filament Extrusion. Dried pellets were used to feed a Thermo Haake PTW16 intermeshing, co-rotating twin-screw extruder by Thermo Haake, Karlsruhe, Germany (screw diameter $D = 16$ mm; L/D ratio = 25, where L is the screw length; rod die diameter 1.80 mm). Filaments with a diameter of about 1.70-1.80 mm were collected by using a take-up unit Thermo Electron Type 002-5341 (Thermo Haake, Karlsruhe, Germany) with a collection rate optimized for the required filament diameter. The main parameters adopted for filament production are summarized in Table 1.

2.2.3 3D-Extruded Fibers. 3D-extruded fibers were properly prepared for mechanical testing, starting from the extruded filament by using a prototype of a 3D printer for high-temperature processing, Sharebot HT Next Generation desktop (Sharebot NG, Nibionno, LC, Italy) through a nozzle diameter of 0.40 mm at a temperature of 270 °C. Fibers of about 70 mm length with a diameter of 1.00 ± 0.05 and 0.62 ± 0.01 mm of PA and PA/CF, respectively, were freely extruded.

2.2.4 3D-Printed Samples Preparation. 3D-printed specimens were produced by feeding the 3D printer Sharebot HT Next Generation desktop (Sharebot NG, Nibionno, LC, Italy). All samples were printed according to the FFF parameters: nozzle diameter 0.40 mm; nozzle temperature 270 °C; bed temperature 110 °C; infill 100%; raster angle $-45^\circ/+45^\circ$; layer height 0.20 mm; and infill speed 40 mm/s. Pictures of the investigated samples, along with indications on the different building orientations are reported in Fig. 1.

2.3 Testing Techniques

2.3.1 Density Measurements. Density measurement of bulk samples (CM and filament) was performed according to the standard ASTM D792-13 (buoyancy method) (Ref 19) in ethanol with at least five replicated specimens for each sample. Apparent density of 3D-printed samples was also determined from direct measurement of weight and volume. The voids

Table 1. Processing parameters for the extrusion of PA and PA/CF filament with the twin-screw extruder

Parameters	PA	PA/CF
Screw speed, rpm	15	15
Zone 1— T_1 , °C	200	200
Zone 2— T_2 , °C	260	260
Zone 3— T_3 , °C	270	270
Zone 4— T_4 , °C	250	250
Head of extruder $T_{5(\text{die})}$, °C	200	200
Pressure, bar	43 ± 3	48 ± 3
Torque, Nm	74 ± 6	44 ± 4

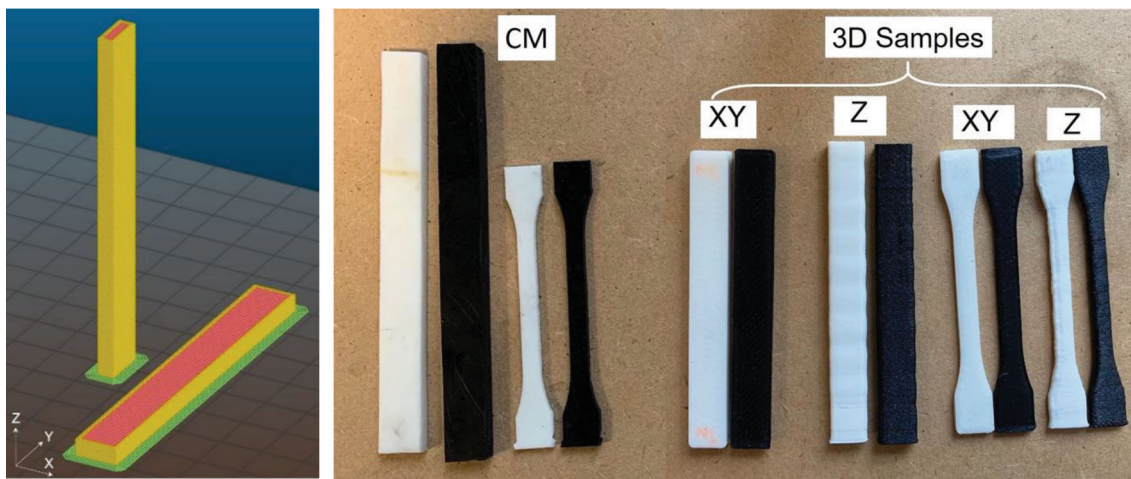


Fig. 1. 3D model with different build orientations (XY and Z); compression-molded (CM) and 3D-printed samples in XY and Z orientations: PA (white color) and PA/CF (black color)

content in filaments and 3D-printed samples was evaluated from the theoretical (rule of mixture) and the experimental density values where compression-molded samples were considered as a reference for a void-free material.

2.3.2 Scanning Electron Microscopy (SEM). Morphology of fracture surface of tested composites was studied by using a Carl Zeiss AG Supra 40 field emission scanning electron microscope (FESEM) at an acceleration voltage of 4 kV.

2.3.3 Differential Scanning Calorimetry (DSC). Differential scanning calorimetry tests were performed by a Mettler DSC 30 calorimeter on samples with a mass of about 10 mg. A thermal cycle of heating-cooling-heating in the range 30–300 °C at a rate of ± 10 °C/min under a nitrogen flow of 100 mL/min was selected. Crystallinity of the samples was calculated in first heating (X_{m1}), cooling (X_c) and second heating (X_{m2}) using the equation:

$$X_{m1,c,m2} = \frac{\Delta H_m - \Delta H_c}{\Delta H_m^0} \times 100/f$$

where ΔH_m and ΔH_c are the integrals of endothermic and exothermic peaks in each scan, respectively, f is the PA matrix content and $\Delta H_m^0 = 196$ J/g is the melting enthalpy of a 100% crystalline PA66 (Ref 20).

2.3.4 Dynamic Mechanical Thermal Analysis (DMTA). Dynamic mechanical thermal analysis tests were performed by a TA Instruments DMA Q800 device (TA Instruments-Waters LLC, New Castle, DE, USA). CM and 3D-printed samples of dimensions $60 \times 5 \times 2$ mm while adopting a constant span length of 35 mm were tested in a temperature range from -100 to 200 °C at a heating rate of 3 °C/min in dual-cantilever mode applying a maximum dynamic strain of 0.05% at a frequency of 1 Hz. Storage modulus (E'), loss modulus (E'') and loss tangent ($\tan \delta$) or damping as a function of the temperature were reported.

2.3.5 Vicat Softening Temperature (VST). Vicat softening temperature was measured by a HDT-VICAT instrument (ATS-Faar S.p.A., Milano, Italy) following ASTM D1525-09 (Ref 21). Three specimens of 4 mm thickness were tested for

each sample, at a heating rate of 120 °C/h under an applied load of 50 N. The upper surface of 3D-printed specimens was examined.

2.3.6 Quasi-static Tensile Test. Uniaxial tensile tests were performed at room temperature by an Instron[®] 5969 electromechanical testing machine equipped with a 50-kN load cell. Fracture properties were evaluated on specimens consisting of (i) extruded filaments (gauge length 100 mm; diameter 1.75 mm) at a crosshead speed of 10 mm/min and (ii) 3D-printed samples, ISO 527 type 1BA dumbbell (gauge length 30 mm; width 5 mm; thickness 2 mm) at crosshead speed 10 mm/min. Tensile properties of 3D-extruded fibers were also determined by using an Instron[®] 5969 electromechanical tester equipped with a load cell of 1 kN. Fiber specimens with a diameter between 0.62 and 1.00 mm and a gauge length of 20 mm were tested at a crosshead speed of 2 mm/min. Elastic modulus of 3D-printed specimens was determined at a crosshead speed of 1 mm/min by an electrical extensometer Instron[®] model 2620-601 with a gauge length of 12.5 mm, whereas the tensile modulus of filament specimens was measured at a crosshead speed of 10 mm/min without an extensometer with a gauge length of 100 mm taking the system compliance into account. For each sample, five specimens were tested. According to the ISO 527 standard (Ref 22), the elastic modulus was determined as a secant value between strain levels of 0.05% and 0.25%.

2.3.7 Flexural Test. Flexural testing (three points bending) was performed according to ASTM D790 (Ref 23) on specimens with a length of 80 mm, width of 10 mm and thickness of 4 mm. The tests were carried out by using an Instron[®] 5969 electromechanical testing machine equipped with a 50-kN load cell at a crosshead speed of 1.70 mm/min on specimens with a span length of 64 mm. For each sample, five specimens were tested.

2.3.8 Charpy Impact Test. Charpy impact tests were carried out at room temperature following ISO 179 (Ref 24) using a CEAST machine equipped with a hammer having a mass of 1.18 kg and setting an initial impact speed of 2.9 m/s with a maximum impact energy of 5 J. The striking nose of the

hammer is characterized by an included angle of 30°. Rectangular samples of 80 × 10 × 4 mm without a notch were tested with a span length of 62 mm. At least five specimens were tested for each sample. The test allowed the measurement of the maximum force reached during the tests (F_{\max}) and the specific energy adsorbed at break (E_{tot}).

2.3.9 Plane-Strain Fracture Toughness and Strain Energy Release Tests. A more in-depth investigation of the fracture behavior of melt-compounded composites was carried out through the linear elastic fracture mechanics methods based on the determination of the plane-strain fracture toughness parameters under mode I, K_{IC} and G_{IC} . An Instron universal testing machine, equipped with a 50-kN load cell, was used. According to ASTM D 5045 standard (Ref 25), single-edge-notched bending samples (SENB), 44 mm long, 10 mm wide and 5 mm thick with a span length of 40 mm, were tested at a crosshead speed of 10 mm/min. Samples were pre-notched with a sharp notch of 5 mm in-depth, with a notch tip radius of less than 10 μm . Critical values of stress intensity factor (K_{IC}) and strain energy release rate (G_{IC}) values were determined on samples of at least five specimens.

2.3.10 Electrical Resistivity Test. The electrical resistance at various temperatures for CM and 3D-printed sheets (30 × 5 × 2 mm) was measured according to a two-probe method by using an ISO-TECH IDM 67 Pocket Multimeter electrometer in a refrigerator (at -16° and +5 °C) and in an oven (at 25 °C, 50 °C, 100 °C and 150 °C). Specimens were painted with a conductive paste at both ends and dried at 60 °C for at least 30 min before testing.

2.3.10.1 Strain Monitoring. The monitoring of the response of electrical resistance changes due to an applied mechanical deformation was performed on CM and 3D-printed composite samples in both short- and long-term experiments performed according to the scheme reported in Fig. 2. ISO 527 1BA specimens with a thickness of 2 mm were tested by using an Instron® 5969 electromechanical testing machine under three loading conditions: (i) quasi-static ramp tensile test (at a deformation rate of 1%/min) up to fracture, (ii) quasi-static ramp tensile test up to 1% strain and (iii) sinusoidal cyclic test. The strain was measured by using an extensometer Instron® model 2620-601 with a gauge length of 12.5 mm. A two-probe method was used for measuring the electrical resistance by a Keithley 6517A high-resistance meter at an applied current of 2 mA. A silver paste was applied on the specimen's surface to ensure a good electrical contact (Fig. 2).

3. Results and Discussion

In the following paragraphs, the results of thermal and mechanical characterization of PA matrix and CF composites will be initially presented, with specific comparison of the different specimens produced by compression molding, filament extrusion and 3D-printing analysis. Then, the specific behavior of different CF composite specimens is detailed in terms of electrical and conductive properties, in view of strain monitoring applications (gauge factor and cyclic tests). The final paragraph is dedicated to a comparative summary of short-fiber thermoplastic composites for the production of 3D-printing items (processing and properties) (Table 2).

3.1 Differential Scanning Calorimetry

The crystallinity of polymers is known to play a significant role on their mechanical properties, such as elastic modulus, fracture toughness, yield strength and thermal resistance. Although 3D-printing parameters (e.g., environment temperature, bed temperature, nozzle temperature, printing speed) were fixed, different parts of 3D-printed specimens were exposed to a different cooling profile (Ref 26). Therefore, it is interesting to investigate the crystallinity of 3D-printed samples in various different positions, such as top, bottom, shell and core (Fig. 3).

The crystallinity in different positions of 3D-printed samples was also analyzed by DSC. The typical DSC diagrams of PA samples are represented in Fig. 3. In the first scan (Fig. 3a), three transitions are clearly visible such as a glass transition, a cold crystallization peak in the interval 90-130 °C and a melting peak in PA-Filament, PA-Top and PA-Bottom samples. The cold crystallization is associated with incomplete crystallization, while the melting peak represents the polymer transforming from a solid to a molten state. The imperfect crystallization of the filament and printed samples could be attributed to the rapid cooling due to a high-temperature difference between the die/nozzle and the ambient air during extrusion. However, no cold crystallization peak was observed on PA from compressing molded samples (at a cooling rate of about 20 °C/min in processing) in the first scan and in the second scan of all samples (at a cooling rate of 10 °C/min in DSC chamber), as shown in Fig. 3(c). In Fig. 4(a), 3D-printed PA/CF sample also shows the different distributions of crystallinity: higher imperfect crystallization at the top and shell and lower in the bottom and core. Moreover, for rapidly cooled samples CFs promoted (i.e., filament and 3D-printed samples) a reduction in crystallization temperature and an increase in crystallization amount as shown in Table 3, thus suggesting a specific role of CF as nucleating agents. Therefore, the crystallization behavior of PA and PA/CF samples was highly dependent on the incorporation of CF and the processing conditions.

3.2 Dynamic Mechanical Thermal Analysis and Vicat Softening Temperature

Dynamic mechanical thermograms of PA and its PA/CF composite samples produced by compression molding and 3D printing are shown in Fig. 5. In Table 4, selected values of storage modulus (E'), peaks of damping or loss tangent ($\tan \delta$) and loss modulus peak (E'') are summarized. It is well evident that storage modulus of CF composites is higher than neat PA matrix below 75 °C for both CM and FFF samples. Moreover, in the case of pure matrix, due to the presence of porosity in the 3D-printed sample, the storage modulus of PA-XY is lower than that of compression-molded samples in the entire temperature range (Fig. 5a). On the other hand, after addition of CF in the PA matrix, the storage modulus of FFF composite sample is higher than that of CM composite sample in the interval -25 °C/+75 °C (between the two transitions), due to carbon fiber orientation; this effect could be directly attributed to the alignment of the filler in the polymeric matrix induced by the 3D-printing process. It is also important to note that storage modulus in tensile DMA was measured at very low dynamic strain 0.05%.

As expected for polyamide, two main damping peaks in all samples are clearly observed in Fig. 5(b). In particular, a first

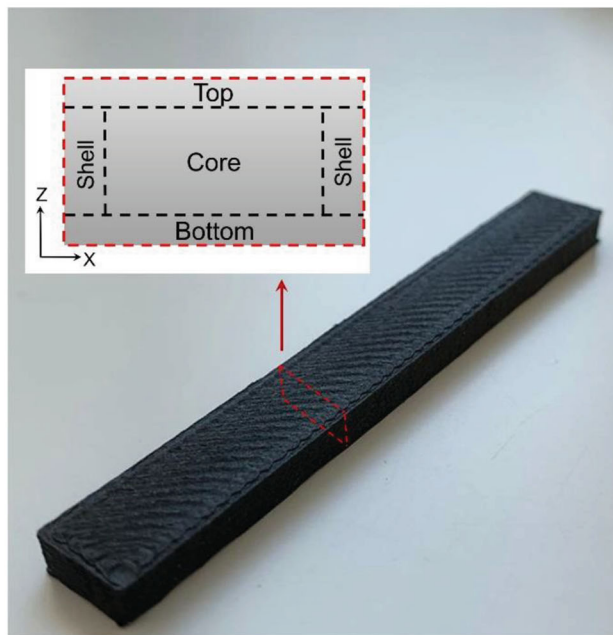
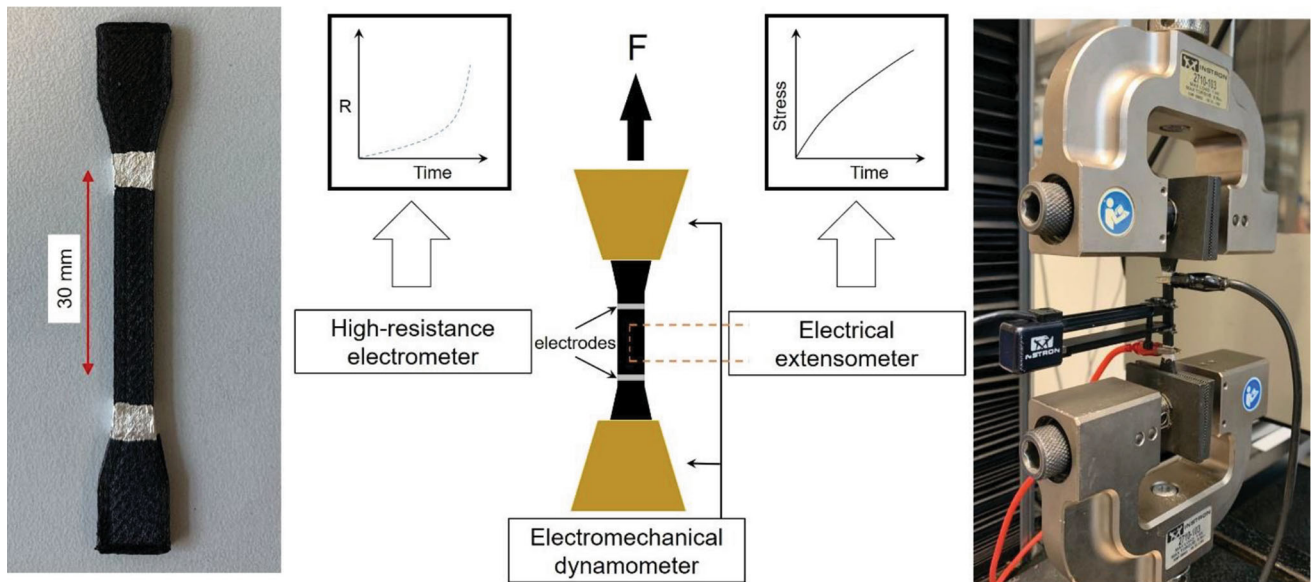


Fig. 2. Schematic of the experimental setup for strain monitoring

peak in the interval $-60\text{ }^{\circ}\text{C}$ to $-53\text{ }^{\circ}\text{C}$ is related to the beta transition (T_{β}) which is attributed to a segmental motion involving nonhydrogen-bonded amide groups (Ref 27). In addition, the glass transition temperature (T_g) is associated with a main (alpha) peak located at about $80\text{-}92\text{ }^{\circ}\text{C}$ for diluent-free samples (Ref 28, 29). The presence of the CFs causes a decrease in the height of both beta and alpha peaks, due to the lower mobility of amorphous phase. In fact, beta peak decreases from 0.035 to 0.025 for both CM and 3D-printed samples, while alpha peak decreases from about 0.25 to 0.15 and from 0.8 to 0.5 for CM and 3D-printed samples, respectively. Moreover, compression-molded samples, due to their lower crystallinity, evidenced an alpha peak with a lower intensity (0.2-0.3) than that of 3D-printed samples (0.7-0.9). In fact, in this latter case, it is also worth noting the increase in modulus above T_g in the range $100\text{-}150\text{ }^{\circ}\text{C}$, due to crystallization of

polyamide PA-XY and PA/CF-XY, in good agreement with DSC results.

Representative thermal curves of Vicat analysis and results of Vicat softening temperature (VST) values are summarized in Fig. 6. For PA-CM, a value of about $191\text{ }^{\circ}\text{C}$ is measured, while 3D-printed samples display lower VST values in the range $171\text{-}178\text{ }^{\circ}\text{C}$ mainly due to the presence of voids and polymer orientations. On the other hand, the effect of carbon fiber (CF) is quite relevant in improving VST values for both CM sample (about $6\text{ }^{\circ}\text{C}$) and especially 3D-printed samples (about $14\text{ }^{\circ}\text{C}$).

3.3 Mechanical Properties

3.3.1 Quasi-static Tensile and Flexural Properties. Quasi-static tensile properties were measured on both filaments and fibers for both PA and PA/CF composites.

Table 2. Selected DSC results (first heating scan): glass transition temperatures (T_{g1}), crystallization peaks (T_{c1} , T_{c2}), crystallization enthalpies (ΔH_{c1} , ΔH_{c2}) melting peak (T_{m1}), melting enthalpy (ΔH_{m1}) and percentage crystallinity (X_{m1}) in PA and PA/CF composites (see Fig. 3a and Fig. 4a)

Samples	First heating							
	T_{g1} , °C	T_{c1} , °C	ΔH_{c1} , J/g	T_{c2} , °C	ΔH_{c2} , J/g	T_{m1} , °C	ΔH_{m1} , J/g	X_{m1} , %
PA-CM	70.8	...	0.0	...	0.0	242.1	40.5	20.7
PA-Filament	69.5	116.0	14.5	188.8	1.0	240.1	49.9	17.6
PA-3D-Top	68.6	111.4	20.0	188.3	2.3	239.5	52.3	15.3
PA-3D-Bottom	72.5	108.5	10.5	184.7	2.4	240.2	51.0	19.4
PA/CF-CM	52.6	...	0.0	...	0.0	234.2	34.0	17.4
PA/CF-Filament	53.8	98.0	14.2	174.6	2.4	233.5	40.6	12.2
PA/CF-3D-Top	54.5	101.2	10.1	177.0	2.4	233.8	40.2	14.1
PA/CF-3D-Bottom	56.7	...	0.0	...	0.0	233.5	40.2	20.5
PA/CF-3D-Core	51.0	97.8	0.3	175.8	3.1	233.5	39.9	18.6
PA/CF-3D-Shell	52.3	100.0	3.2	171.5	5.7	233.3	39.6	15.7

First (c1) and second (c2) crystallization peak (Fig. 3a and 4a)

Table 3. Selected DSC results (cooling and second heating scan): crystallization temperature (T_c), glass transition temperatures (T_{g2}), melting peak (T_{m2}), melting enthalpy (ΔH_{m2}) and percentage crystallinity (X_c and X_{m2}) in PA and PA/CF composites (see Fig. 3b, c and Fig. 4b, c)

Samples	Cooling		Second heating			
	T_c , °C	X_c , %	T_{g2} , °C	T_{m2} , °C	ΔH_{m2} , J/g	X_{m2} , %
PA-CM	181.6	17.8	73.6	237.3	36.3	18.5
PA-Filament	184.5	17.5	73.5	235.9	35.9	18.3
PA-3D-Top	184.9	17.7	71.3	235.4	36.3	18.5
PA-3D-Bottom	184.9	17.8	74.1	235.7	35.6	18.2
PA/CF-CM	182.7	18.3	66.5	231.4	27.7	19.8
PA/CF-Filament	181.2	19.0	66.5	231.8	28.3	20.2
PA/CF-3D-Top	181.2	18.8	65.6	231.0	27.1	19.3
PA/CF-3D-Bottom	181.6	18.8	66.3	230.8	27.5	19.7
PA/CF-3D-Core	181.6	19.0	65.6	230.4	27.1	19.4
PA/CF-3D-Shell	182.0	18.7	65.4	230.2	27.7	19.8

Representative stress–strain curves of filaments of PA and PA/CF composites are reported in Fig. 7(a). The main results are summarized in Table 5. An almost equivalent mechanical behavior can be observed for the extrudates (both filament and fibers) with no direct dependence on the polymer orientation. Tensile modulus and density of filaments are similar to those of fibers.

The presence of carbon fibers reduced the ductility and porosity of PA. Interesting, the strength of PA/CF filament and fiber is significantly higher than that of PA. A porosity content of PA/CF composite filaments was calculated to be about 5.4 vol.%. The presence of porosity is also confirmed by the SEM micrographs reported in Fig. 8. Carbon fibers can be observed to be homogeneously distributed in the polymer and highly oriented along the extrusion flow direction.

Stress–strain curves of CM and 3D-printed samples are shown in Fig. 7(b), and the resulting mechanical parameters are summarized in Table 6. Compression-molded samples evidenced a tensile modulus higher than the corresponding 3D-printed samples, even in the case of CF composite; it should be noted that tensile modulus measured with extensometer was determined in a wider strain level 0.05–0.25%, with respect to DMA. Therefore,

the role of residual cavity seems to prevail on carbon fiber orientation at higher deformation of 3D-printed samples. Comparing the effect of different 3D-printing patterns, it is worth noting that the elastic modulus of PA/CF composites increased up to 147% and 4% above that of unfilled PA at the orientation of XY and Z, respectively. The highest strength can be observed in PA/CF-XY sample owing to the reinforcing effect of carbon fibers, whereas, as expected, the strength of Z-printed samples is lower due to the weakness of interlayer bonding. As a side effect, the elongation at break of FFF composites samples was significantly reduced by the presence to the CF.

Flexural properties (i.e., strength and stiffness) result from the combined effects of material properties under various loading modes such as tensile, compressive and shear. Standard stress–strain curves of the printed and molded specimens, obtained by quasi-static three-point bending tests, are represented in Fig. 9(a).

The specific values of the flexural properties, density and void content are summarized in Table 7. The flexural strength and modulus of the 3D-printed samples were compared to those of the compression-molded neat PA samples. The compression-molded samples of PA exhibited slightly higher mechanical

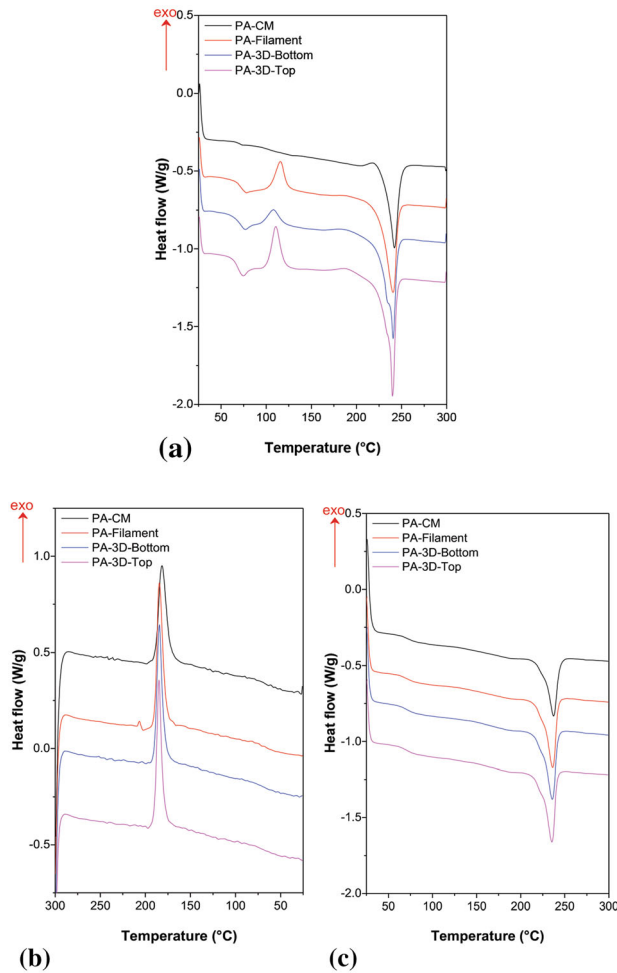


Fig. 3. Scheme of 3D-printed section and DSC curves of PA from compression-molded, filament and 3D-printed samples: (a) first heating, (b) cooling and (c) second heating scan

strength and elastic modulus than that of PA-XY due to the presence of void and the effect orientation of carbon fibers. The PA/CF composites showed higher strength and elastic modulus in comparison with PA samples for both CM and 3D-printed samples in XY orientation. For Z-printed samples, flexural modulus of CF composite was slightly lower than that of neat PA (2.10 vs. 2.40 GPa), thus indicating a certain reduction in the interlayer rigidity after addition of CF. On the other hand, PA and PA/CF evidenced a similar strength (34–36 MPa), but a slightly higher deformation at break was found for PA/CF-XY.

The morphology of compression-molded and 3D-printed samples was investigated through SEM observation. In Fig. 10, SEM images reveal that CFs were randomly orientated in the polymer matrix for CM-samples, but highly oriented in the XY plane for 3D-printed samples. Tensile elastic modulus and flexural modulus of PA/CF-CM are slightly higher than those of PA/CF-XY because of the counteracting effects of voids and orientation of CFs. In general, the void formation in fiber-reinforced composites produced by 3D printing is designated by: (1) inter-beads voids created by physical gap at inner layer and interlayer, (2) inner-bead voids generated by the escaping

gas and (3) cylindrical voids formed by fiber pullout. The void content in PA/CF-XY is about 7.5%; however, the inter-beads voids formed during the 3D-printing process are less visible, as shown in Fig. 10(c) and (d). Similar morphology of PA/CF 3D-printed samples was found in previous studies (Ref 15, 16).

3.3.2 Charpy Impact Strength. In Fig. 11, representative load–displacement curves of the investigated materials tested under impact conditions are reported, and the most important results are summarized in Table 8. Due to their high toughness, PA samples produced by CM did not break under the selected testing conditions; however, PA-XY sample manifested an impact strength of 111 kJ m^{-2} due to the presence of voids in the samples. The introduction of CF for both PA-CM and PA-XY samples caused a slight increase in the maximum force, but a decrease in the specific energy adsorbed at break (E_{tot}). This behavior is probably due to non-optimal fiber–matrix interfacial adhesion and fiber length. The impact strength of PA-CM is 48.9 kJ m^{-2} , which is consistent with the value reported in the technical datasheet. Our data are higher than the data reported by Liao et al. (Ref 15) of 22.5 kJ m^{-2} and 24.8 kJ m^{-2} for PA and PA/CF 10 wt.%, respectively. The presence of CFs has two

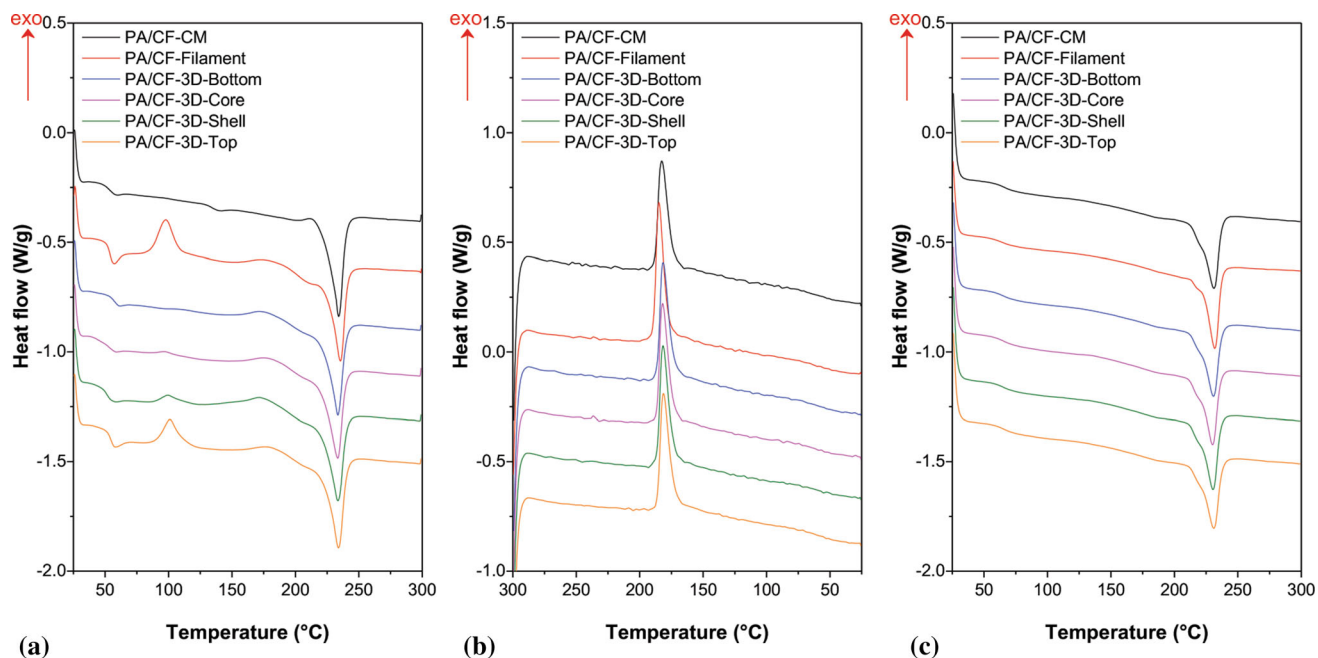


Fig. 4. DSC curves of PA/CF of compression-molded, filament and 3D-printed samples: (a) first heating, (b) cooling and (c) second heating scan

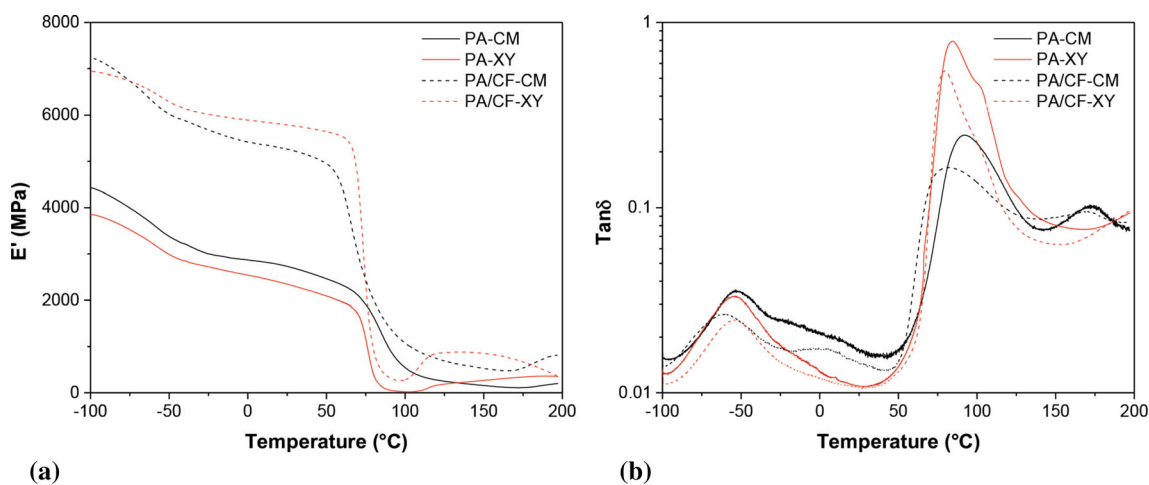


Fig. 5. Dynamic mechanical thermograms of compression-molded (CM) and 3D-printed samples of PA/CF composites: (a) storage modulus (E') and (b) loss tangent ($\tan \delta$)

Table 4. Selected dynamic mechanical properties of PA and PA/CF composites as measured on compression-molded (CM) and 3D-printed specimens

Samples	Storage modulus					Damping peaks		Loss modulus peak	
	at $-25\text{ }^{\circ}\text{C}$, MPa	at $0\text{ }^{\circ}\text{C}$, MPa	at $25\text{ }^{\circ}\text{C}$, MPa	at $100\text{ }^{\circ}\text{C}$, MPa	at $150\text{ }^{\circ}\text{C}$, MPa	$T_{g,\beta}$, $^{\circ}\text{C}$	$T_{g,\alpha}$, $^{\circ}\text{C}$	E''_{peak} , MPa	T_{peak} , $^{\circ}\text{C}$
PA-CM	3002	2869	2730	546	157	- 53.3	92.1	273	84.7
PA-XY	2720	2540	2345	23	267	- 53.5	84.4	382	72.0
PA/CF-CM	5677	5415	5261	1071	527	- 59.6	80.1	398	71.4
PA/CF-XY	6015	5891	5788	280	850	- 54.3	79.6	974	74.5

opposite effects on the fracture strength: to increase the defect density and to prevent the crack propagation in particular when fibers are perpendicular to crack direction. In another work (Ref 14), the addition of CF and GF at a content of 5-15 wt.% in PEEK was found to progressively reduce its impact strength.

It is interesting to note that PA and PA/CF composites produced by 3D printing in Z orientation showed the lower values of impact strength, because impact loading was parallel to the interlayer of samples. In addition, PA/CF-Z sample exhibited similar or even higher total impact energy compared to PA-Z sample. This result represents an enhancement of

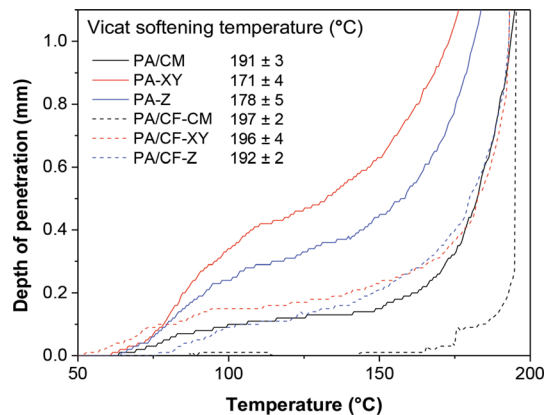


Fig. 6. Vicat softening curves and VST results of compression-molded (CM) and 3D-printed samples

Table 5. Diameter, tensile properties, density and void content of filaments and fibers produced by twin-screw extruder or by 3D printer, respectively

Samples	Diameter, mm	E , GPa	σ_y , MPa	σ_b , MPa	ϵ_b , %	Density, g/cm ³	Void, %
PA-Filament	1.82 ± 0.04	2.77 ± 0.07	74.4 ± 1.8	52 ± 2	165 ± 11	1.165 ± 0.003(a)	0.4 ± 0.2
PA-Fiber	1.00 ± 0.05	2.57 ± 0.18	70.9 ± 3.0	...	> 200	1.160 ± 0.004(a)	1.0 ± 0.3
PA/CF-Filament	1.72 ± 0.04	10.57 ± 0.47	...	133.4 ± 3.4	2.2 ± 0.1	1.206 ± 0.010(a)	5.4 ± 0.8
PA/CF-Fiber	0.62 ± 0.01	11.35 ± 0.47	...	155.2 ± 7.5	2.6 ± 0.4	1.234 ± 0.007(a)	3.2 ± 0.5

(a) Density from buoyancy method.

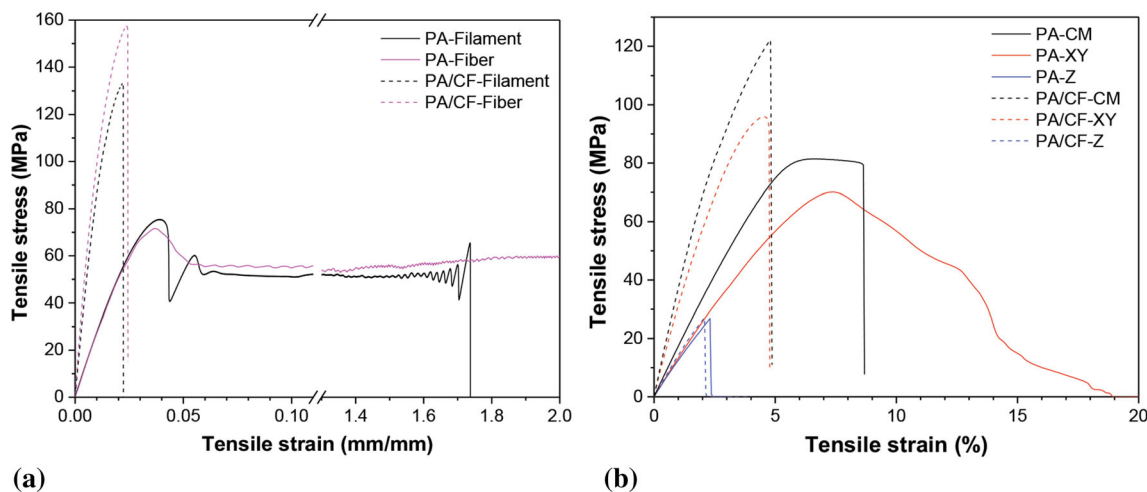


Fig. 7. Representative tensile stress-strain curves of (a) filaments and fibers and (b) compression-molded and 3D-printed samples

interlayer adhesion in 3D printing, and it is in line with the findings of the tensile and flexural tests. In addition, Ding et al. (Ref 30) also reported a similar effect of build orientation (X vs. Z) on the impact strength of 3D-printed PA/CF composites.

3.3.3 Plane-Strain Fracture Toughness. According to ASTM standard D5045, the critical stress intensity factor (K_{IC}) and the critical strain energy release rate (G_{IC}) were calculated by using the following equation:

$$K_Q = \frac{P_Q}{B\sqrt{W}}f(x) \quad (\text{Eq 1})$$

where

$$f(x) = 6x^{1/2} \frac{[1.99 - x(1-x)(2.15 - 3.92x + 2.7x^2)]}{(1+2x)(1-x)^{3/2}} \quad (\text{Eq 2})$$

B is the specimen thickness, W is the specimen width, a is the length of a notch obtained by a sharp razor blade and x is a ratio of crack length to specimen width. K_Q is an apparent fracture toughness, where P_Q is the load corresponding to a line with a compliance 5% higher than that of the tangent line (Fig. 12a). When the maximum load (P_{max}) was in between the two straight lines, P_{max} was used to calculate the apparent fracture toughness (K_Q). When P_{max} was outside the two straight lines, as shown in Fig. 12(a), P_Q was used to calculate K_Q . Then, K_Q value is considered as equal to K_{IC} if the following conditions are satisfied:

$$\frac{P_{max}}{P_Q} < 1.1 \quad (\text{Eq 3})$$

Table 6. Tensile properties of compression-molded (CM) and 3D-printed samples

Samples	E , GPa	σ_y , MPa	σ_b , MPa	ϵ_b , %	TEB, MJ/m ³
PA-CM	3.67 ± 0.22	80.4 ± 1.9	...	8.5 ± 1.3	4.81 ± 0.87
PA-XY	3.18 ± 0.14	71.4 ± 1.8	6.85 ± 0.79
PA-Z	2.80 ± 0.15	...	26.0 ± 4.3	2.4 ± 0.4	0.34 ± 0.12
PA/CF-CM	10.13 ± 0.62	...	119.3 ± 4.7	4.6 ± 0.5	3.24 ± 0.48
PA/CF-XY	7.87 ± 0.23	...	95.7 ± 1.9	5.0 ± 0.6	3.00 ± 0.51
PA/CF-Z	2.90 ± 0.21	...	27.8 ± 3.2	2.2 ± 0.3	0.34 ± 0.09

TEB tensile energy to break

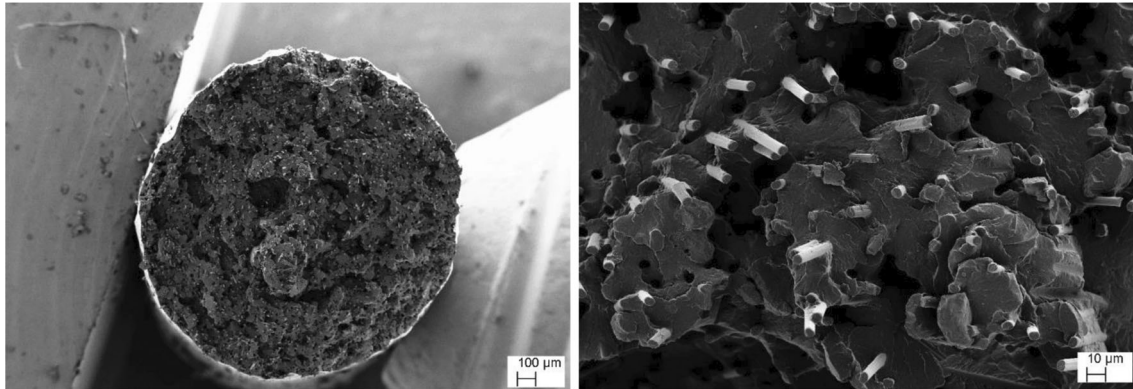


Fig. 8. FESEM micrographs of PA/CF filament

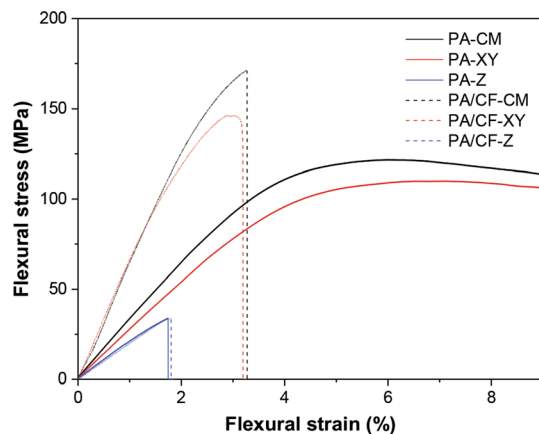


Fig. 9. Representative flexural stress–strain curves of compression-molded (CM) and 3D-printed samples (XY and Z)

$$B, a, (W - a) > 2.5 \left(\frac{K_Q}{\sigma_y} \right)^2 \quad (\text{Eq 4})$$

where σ_y is the tensile yield stress. In this case, the yield stress of each sample was taken from the experimental values of the quasi-tensile test. From the obtained data, Eq 3 is satisfied for all samples, except for PA-CM. However, Eq 4 is satisfied for compression-molded samples, but not for 3D-printed samples. Therefore, instead of K_{IC} , an apparent fracture toughness (K_Q) is reported. The apparent strain energy release rate (G_Q) was evaluated from the following equation:

$$G_Q = \frac{U}{BW\phi} \quad (\text{Eq 5})$$

where U is the strain energy obtained from the load–displacement curve (area under the curve until P_Q) and ϕ is the energy calibration factor according to ASTM D5054.

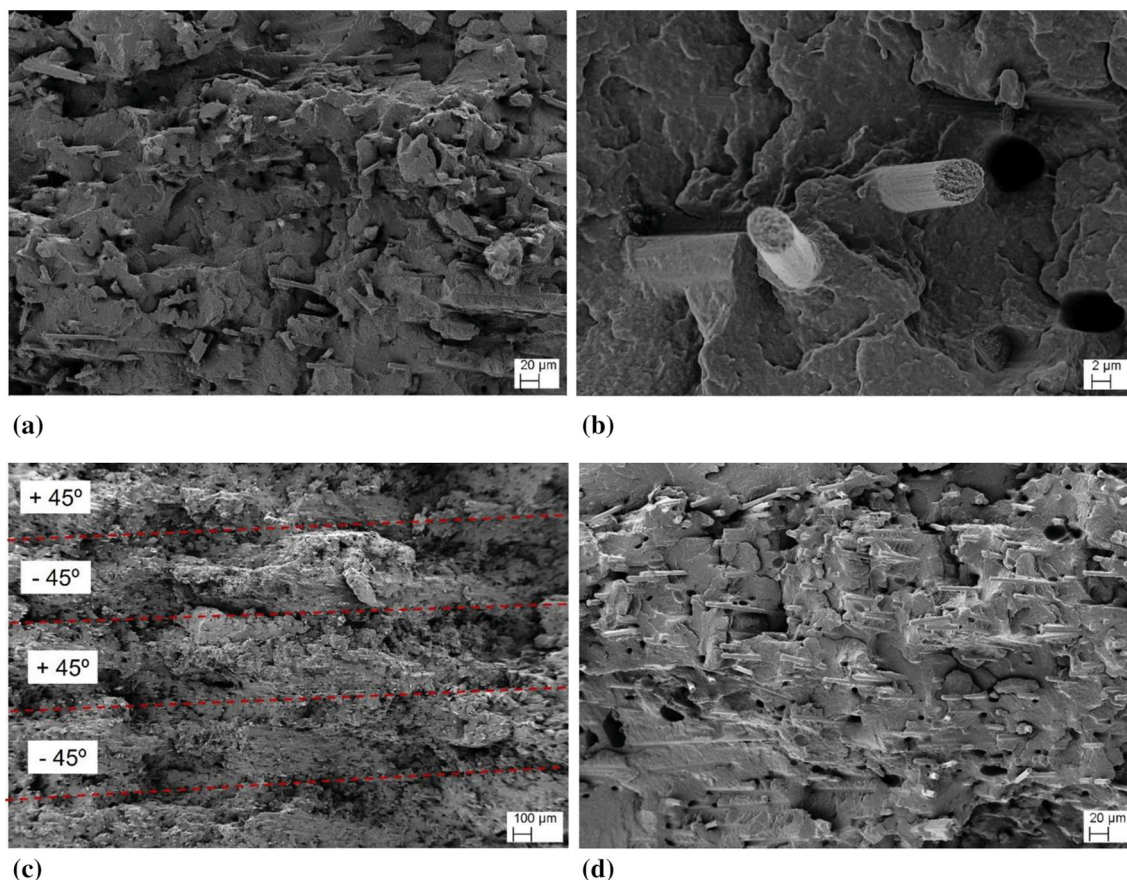
Table 9 summarizes the fracture responses of PA and PA/CF specimens made by CM and FFF process (XY and Z orientation). PA-CM is a highly ductile sample, resulting invalid for the measurement technique because P_Q/P_{max} is higher than 1.1. A typical value of apparent critical stress intensity factor or fracture toughness (K_Q) of PA-XY and PA-Z samples is about 5.6 and 1.8 MPa m^{1/2}, respectively, depending on build orientation from 3D printing. Interestingly, the effect of CF in CM and XY-orientation samples promotes stiffness but reduces the ductility of materials, as shown in Fig. 12(b). PA/CF-XY sample exhibited slightly higher values of K_Q and G_Q in comparison with PA/CF-CM. This characteristic could be attributed to the orientation of CFs and voids in 3D-printed samples. The latter can act as obstacles for crack propagation. Fracture toughness of ABS/CF from 3D printing was also reported to be improved by adding CF up to 5 wt.% in ABS (Ref 31). On the other hand, similarly to what observed for tensile, flexural and impact properties, PA-Z and PA/CF-Z samples manifest lower fracture toughness due to the weak interlayer strength. However, K_Q and G_Q of PA/CF-Z parts are slightly higher in comparison with that of PA-Z sample.

SEM micrographs of the cross-section of PA/CF-XY samples provided more information on the fracture mechanisms. Figure 13 reports SEM images showing details of the crack propagation surface of PA/CF composite from 3D printing. In

Table 7. Flexural properties, density and void content of compression-molded (CM) and 3D-printed samples

Samples	E_p , GPa	σ_m , MPa	ϵ_m , %	Density, g/cm ³	Void, %
PA-CM	3.30 ± 0.08	122 ± 3	6.0 ± 0.2	1.170 ± 0.001 (a)	...
PA-XY	2.71 ± 0.05	110 ± 5	6.7 ± 0.3	1.082 ± 0.012 (b)	7.5 ± 1.1
PA-Z	2.40 ± 0.23	36 ± 4	1.5 ± 0.3	1.072 ± 0.022 (b)	8.3 ± 1.9
PA/CF-CM	6.86 ± 0.45	173 ± 13	3.4 ± 0.4	1.275 ± 0.001 (a)	...
PA/CF-XY	6.52 ± 0.23	142 ± 8	2.9 ± 0.1	1.153 ± 0.012 (b)	9.6 ± 0.9
PA/CF-Z	2.10 ± 0.18	34 ± 2	1.8 ± 0.2	1.096 ± 0.024 (b)	14.0 ± 1.9

(a) Density from buoyancy method.
(b) Apparent density.

**Fig. 10.** FESEM micrographs of flexural PA/CF composites: (a, b) compression-molded and (c, d) 3D-printed samples (XY orientation)

general, the results highlighted that CFs were highly oriented along the 3D-printing flow direction, and the voids generated interlayers are not visible due to a good compatibility of the polymer with the fiber surface.

3.4 Electrical Resistivity and Strain Monitoring

The volume electrical resistivity of PA/CF-CM and PA/CF-XY sample was measured at various temperatures from -16 °C up to 150 °C. The resulting average values are reported in Table 10, whereas the single specimens are presented in Fig. S2. Compression-molded samples evidenced an almost independency on temperature; the large standard deviation depends on the difference between each single specimen, whose average values range between 11 and

$17 \Omega \text{ cm}$ (Fig. S2a). On the other hand, the resistivity of PA/CF-XY decreases from $1.7 \times 10^4 \Omega \text{ cm}$ to $0.7 \times 10^4 \Omega \text{ cm}$ when temperature increases up to 100 °C (see details in Fig. S2b).

In order to investigate the effect of applied strain on the conductivity behavior, CM and 3D-printed composite samples were tested under various loading modes. Following the approach developed for study the strain monitoring of ABS carbon nanotubes samples (Ref 32), the resistivity and the initial absolute resistance of various PA/CF samples were simultaneously monitored by a two-probe contact method. Stress-strain behavior and relative electrical resistance variation (R/R_0) during quasi-static tensile tests are reported in Fig. 14. Tensile stress applied to samples caused a progressive increment in the relative change of electrical resistance (R/R_0)

until the fracture point, with an exponential trend in the case of 3D-printed samples. This behavior could be explained by the destruction of percolating paths forming the conducting network of CFs, in particular above 3%. In order to shed more light on the behavior at lower deformation, the relative change in electrical resistance (R/R_0) of PA/CF-CM and PA/CF-XY

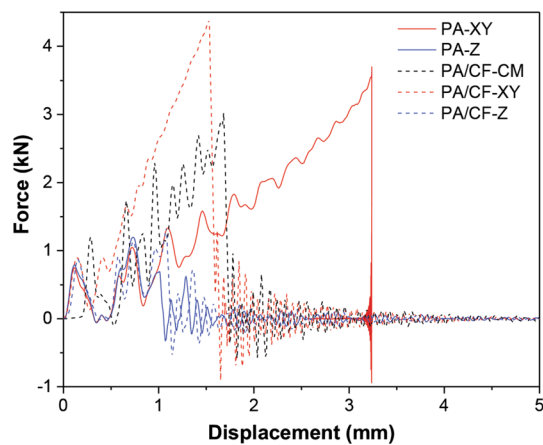


Fig. 11. Representative force–displacement curves obtained in the Charpy impact tests of CM and 3D-printed samples (XY and Z)

Table 8. Charpy impact test results of compression-molded (CM) and 3D-printed samples

Samples	F_{max} , kN	E_{tob} , kJ m^{-2}
PA-CM	NB	NB
PA-XY	3.84 ± 0.12	111 ± 2
PA-Z	1.14 ± 0.14	7.7 ± 2.2
PA/CF-CM	2.85 ± 0.31	48.9 ± 4.5
PA/CF-XY	4.50 ± 0.20	66.1 ± 1.2
PA/CF-Z	1.37 ± 0.15	10.6 ± 0.6

NB, not break

composite upon ramp strain measured by an electrical extensometer up to 1% has been investigated. The results of all the five specimens for each sample are reported in Fig. 15. The tensile stress applied to samples causes an increment in the relative change in electrical resistance (R/R_0). It is important to note that PA/CF-XY samples are more sensitive to strain change than PA/CF-CM due to the difference of morphology (i.e., CFs orientation and the void content). For example, at a strain of 0.5%, R/R_0 of PA/CF-XY sample is about 2.5 ± 0.2 (Fig. 15b), while PA/CF-CM is about 1.04 ± 0.01 (Fig. 15a).

A relatively long period with continuous stress or cyclic loading at the low level of deformation was selected to collect more information on the potentiality of strain monitoring applications of PA/CF composites. Due to the difference in change in resistivity level, the variation of electrical resistance during 50 cycles was detected in the strain range of $0.1\% < \epsilon < 0.5\%$ for PA/CF-XY samples. Results on selected samples are depicted in Fig. 16, while all samples are detailed in Fig. S3. The resistance difference decreases with the number of cycles, as derived from dynamic mechanical effect on the composite in 3D structure. In fact, piezoresistivity progressively seems to decrease in cyclic strain. This characteristic could be attributed to the re-organization of conductive paths, due to possible rearrangement, rotations and reorientation, of the 1D structure of CFs forming the electrical network. This behavior was also observed in ABS carbon nanotubes composites (Ref 32). An apparent stabilization of the resistance decay (electrical resistance change) has been observed in the last 10 cycles, as shown in Fig. 16(b) for PA/CF-XY, respectively. With the purpose to evaluate the stability of strain monitoring, the effect of low cyclic strain has been followed at each step of the cycle by the evaluation of a gauge factor, as previously described (Ref 32). As summarized in Fig. 16(c), the gauge factor calculated as average of three different specimens (Fig. S3) evidenced a stabilized value of about 65 ± 5 in long-term testing (after 20 cycles of dynamic strain).

3.5 Comparative Summary on 3D-Printed Materials with Short Carbon or Glass Fibers

A final overview of studies on 3D printing with engineering plastics containing short carbon or glass fibers is detailed in

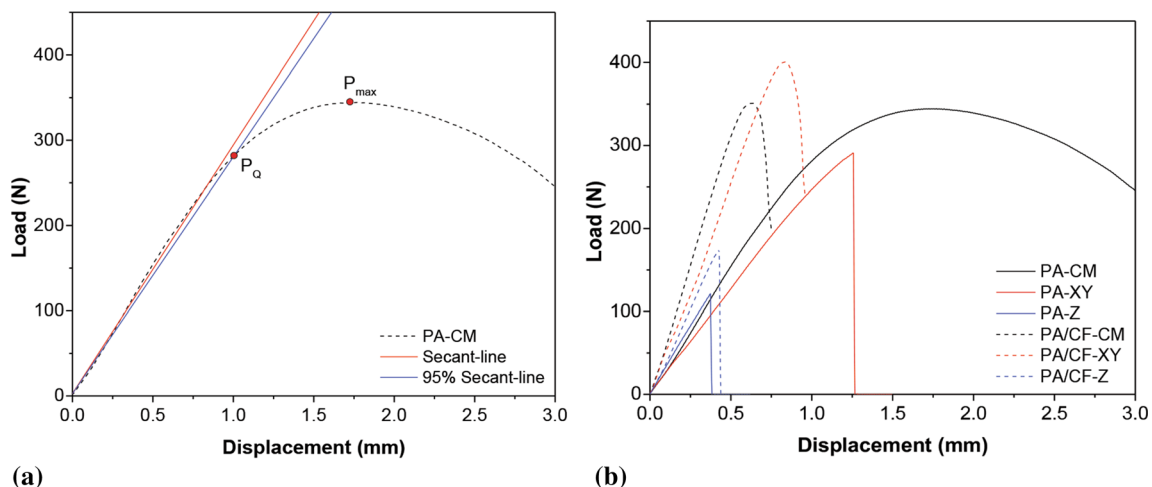


Fig. 12. (a) Representative plot of PA-CM for fracture load calculation strategy; (b) representative load–displacement curves of CM and 3D-printed samples (XY and Z) from the flexural test for the determination of K_Q and G_Q

Table 9. Apparent stress intensity factor (K_Q) and apparent strain energy release rate (G_Q) values of compression-molded (CM) and 3D-printed samples

Samples	P_{max}/P_Q	Verification Eq 4	K_Q , MPa m ^{1/2}	G_Q , kJ m ⁻²
PA-CM	1.22 ± 0.01	NV	NV	NV
PA-XY	1.04 ± 0.03	No	5.58 ± 0.48	11.5 ± 1.5
PA-Z	1.00	No	1.81 ± 0.55	1.15 ± 0.72
PA/CF-CM	1.06 ± 0.02	Yes	6.62 ± 0.42	5.26 ± 0.80
PA/CF-XY	1.01 ± 0.01	No	8.07 ± 0.24	8.04 ± 0.63
PA/CF-Z	1.00	No	3.48 ± 0.54	2.40 ± 0.46
NV, not valid				

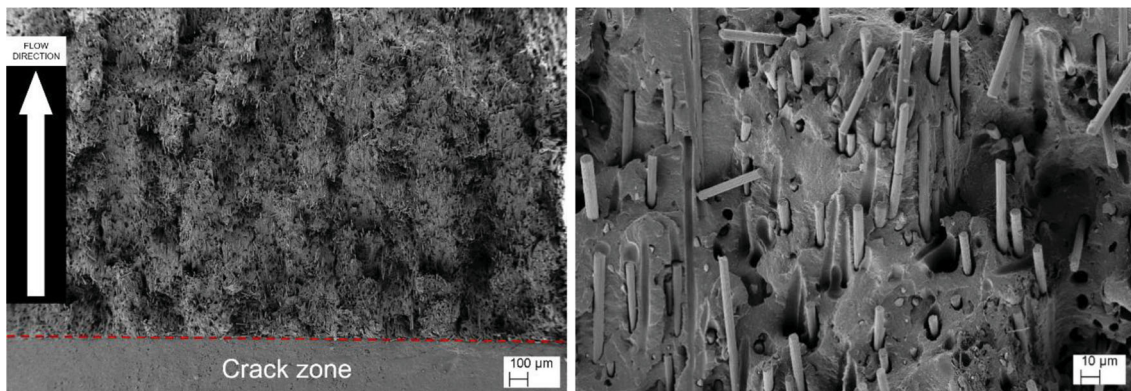


Fig. 13. FESEM micrographs of tested fracture 3D-printed PA/CF samples (XY orientation) after determination of K_Q and G_Q

Table 10. Electrical volume resistivity ρ (Ω cm) in average values from two-probe method at different temperatures of compression-molded (CM) and 3D-printed samples

Samples	Resistivity, Ω cm					
	$T = -16$ °C	$T = 5$ °C	$T = 25$ °C	$T = 50$ °C	$T = 100$ °C	$T = 150$ °C
PA/CF-CM	13.4 ± 3.7	13.4 ± 4.3	13.3 ± 4.1	14.9 ± 4.0	14.5 ± 2.6	14.3 ± 4.5
PA/CF-XY	$(1.7 \pm 0.6) \times 10^4$	$(1.6 \pm 0.6) \times 10^4$	$(1.5 \pm 0.5) \times 10^4$	$(1.1 \pm 0.6) \times 10^4$	$(0.7 \pm 0.2) \times 10^4$...

Table 11. These recent data have been grouped in dependence on the polymer matrix at increasing maximum application temperature, in particular (i) degradable polyester PLA (T_g of about 55 °C); (ii) amorphous copolymers ABS (T_g of about 105 °C); (iii) semicrystalline polymers, PP, PEEK and PA for higher temperature. Commercial filaments were utilized in some studies, while others composite filaments were produced by mixing of carbon fibers (typically ~ 0.1-0.2 mm) at different contents and various thermoplastics before extrusion. The presence of carbon fibers is reported to provide significant reinforcement in thermoplastic polymers, such as PLA, ABS, PP, PEEK and PA. Raster angle and build direction were found the main FFF parameters influenced on the mechanical

properties of 3D-printed samples (see details in Table 11). In most works, carbon fibers are reported to be oriented in deposited flow direction of 3D printing. The samples produced with a raster angle of $[0^\circ]$ evidenced the highest tensile strength and modulus compared to the ones with $[0^\circ/90^\circ]$ and $[\pm 45^\circ]$ angle orientation (Ref 33, 34). According to previous studies, Z-strength of 3D-printed parts was determined as 14-20 MPa for PLA/CF composite (Ref 30) and 10-18 MPa for ABS/CF composite (Ref 35). In our work, we found a Z-strength is about 26-28 MPa for PA/CF composite. On the other hand, an interlayer shear strength of about 15.2 MPa for PA/CF (Ref 11) and 14.5 MPa for ABS/CF composite (Ref 34) was measured. Other researchers reported impact strength in XY plane of about

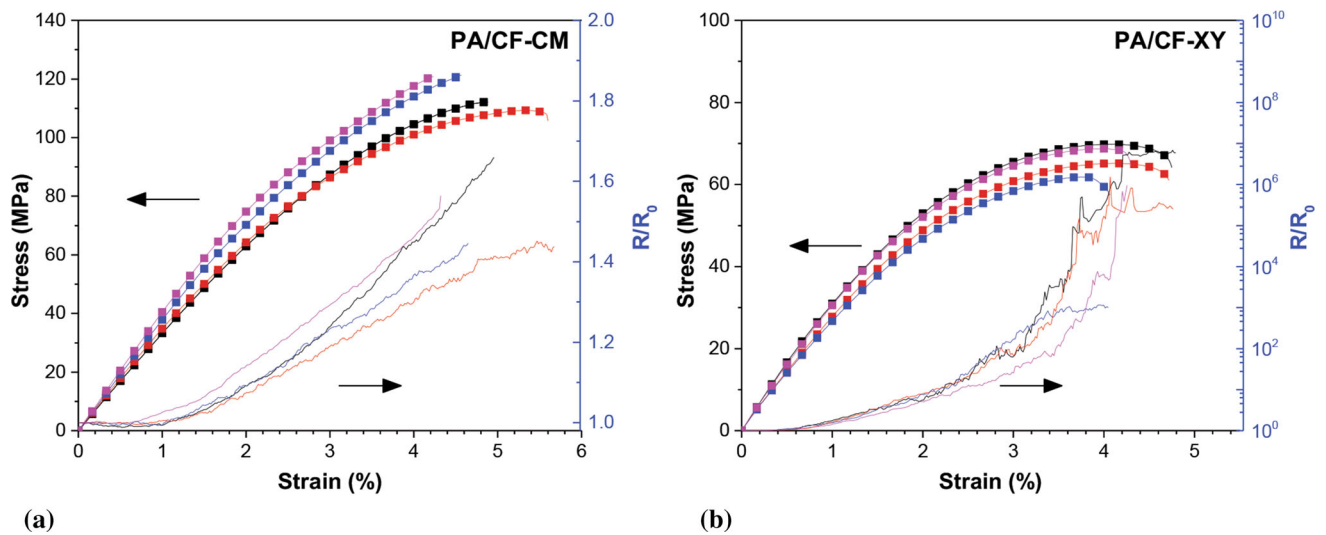


Fig. 14. Mechanical and electrical (R/R_0) response of (a) PA/CF-CM and (b) PA/CF-XY composites of all the tested samples in the fracture test

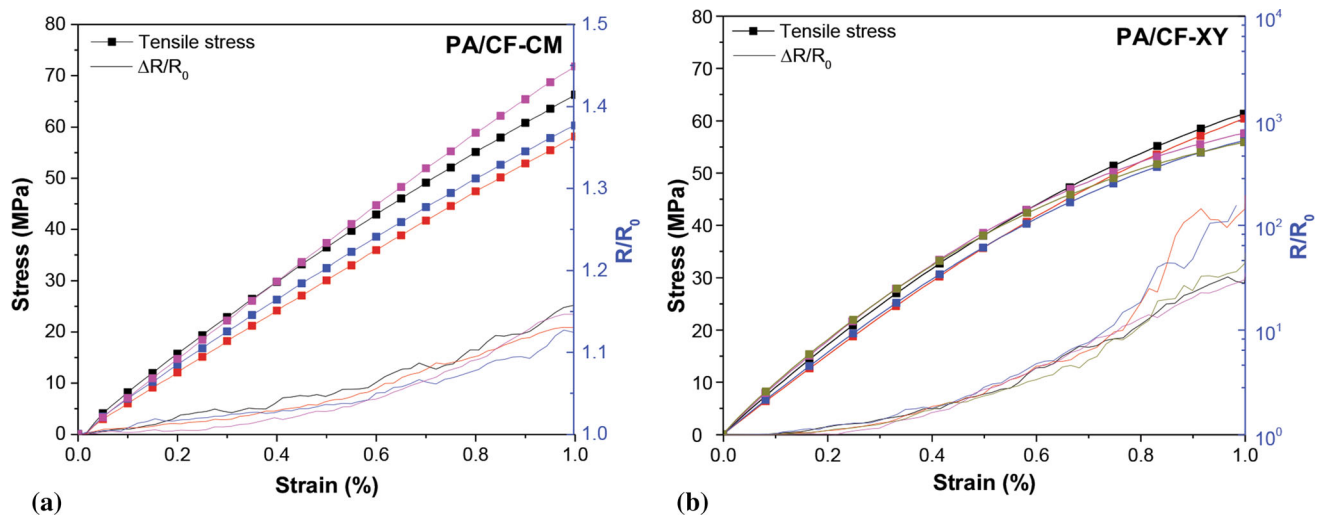


Fig. 15. Mechanical and electrical (R/R_0) response of (a) PA/CF-CM and (b) PA/CF-XY composites of all the tested specimens with extensometer

5.5-7.5 kJ/m^2 for PP/CF (Ref 13), whereas higher values of 18-25 kJ/m^2 and 12-25 kJ/m^2 were found for PEEK/CF (Ref 14) and for PA/CF (Ref 15), respectively. Fracture toughness characteristics of 3D-printed composites have apparent/critical stress intensity factor (K_Q) of 2.9-3.2 $\text{MPa m}^{1/2}$ and strain energy release rate (G_Q) of 3.2-6.2 kJ/m^2 for PLA/CF (Ref 31), but lower value of $G_Q = 3.09 \text{ kJ/m}^2$ for ABS/CF (Ref 36). It is worth noting that in this work $K_Q = 5.6 \text{ MPa m}^{1/2}$

and $G_Q = 11.5 \text{ kJ/m}^2$ were obtained for 3D-printed PA/CF samples. Moreover, for practical applications in temperature, the maximum in-service temperature is expected to increase according to the following order: PLA < ABS < PP < PA < PEEK. According our recent findings, i.e., Vicat test, the suggested applications of 3D-printed PA/CF specimens, either XY or Z orientation, should be considered up to about 150-170 $^\circ\text{C}$.

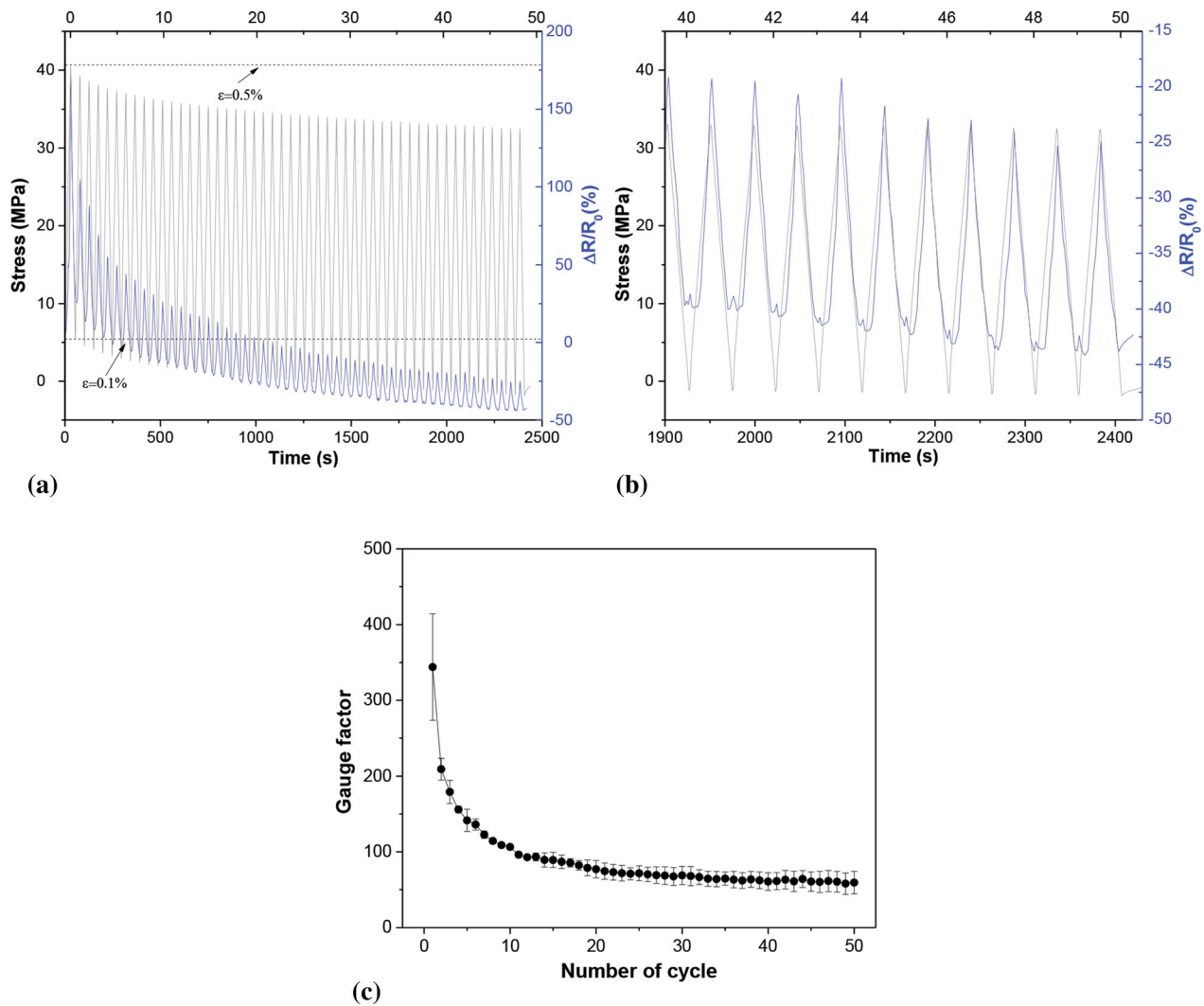


Fig. 16. Piezoresistivity of the PA/CF-XY samples. Experimental results during (a) 50 strain cycles under tensile loading between 0.1 and 0.5% strain, (b) detail of the last ten cycles and (c) gauge factor (average value of three specimens—see Supplementary Fig. S3)

4. Conclusions

High-temperature performance PA and PA/CF composites were extruded into filaments for fused filament fabrication. The 3D-printed parts were successfully produced in XY and Z orientation (extrusion nozzle at 270 °C, bed temperature at 110 °C). The properties of parts from 3D printing were compared with compression-molded samples to study their mechanical (i.e., tensile, flexural, Charpy impact strength and fracture toughness), electrical and piezoresistivity characteristics. The following conclusions can be drawn based on the research results:

1. The elastic modulus and strength of 3D-printed samples are slightly lower than those of compression-molded samples. The tensile performance is 34% for the tensile strength and 147% for the tensile stiffness in comparison with the neat PA. From the flexural behavior point of view, PA/CF-XY samples revealed an increase in average flexural strength and stiffness of 29% and 140%. 3D-printed parts of PA and PA/CF composites in Z-strength have about 26–28 MPa in tensile and 34–36 MPa in flex-

ural mode. In addition, the PA/CF composites from compression molding seemed to have lowered the impact strength and fracture toughness compared to pure PA samples. The ductility, impact strength and fracture toughness of PA/CF samples from 3D printing were lower than those of PA samples. However, the fracture toughness of 3D-printed PA/CF composites was found to be higher in comparison with that of neat PA samples in both XY and Z build orientation.

2. The resistivity of compression-molded PA/CF composite is about 13–15 Ω cm in the temperature range from -16 °C to 100 °C, while the resistivity of PA/CF-3D-printed samples is higher and gradually decreases from 1.7×10^4 Ω cm to 0.7×10^4 Ω cm in the same temperature interval. The piezoresistivity tests revealed that a detectable resistance change occurs in both CM and 3D-printed PA/CF composite samples once strained in tension. Exponential resistance–strain relationships were observed for the elastic region of deformation. Due to different morphologies, 3D-printed samples have significant high resistance change with a gauge factor of about 65 ± 5 .

Table 11. Summary of reported mechanical data of short carbon and glass fiber thermoplastic composites in 3D printing, as function of orientation

Matrix	Reinforcement	Manufacturing technique	Type of fiber reinforcement and amount	Mechanical properties			Detail and comments	Study
				Tensile strength, MPa	Tensile modulus, GPa			
PLA	Short carbon fiber ($L = 60 \mu\text{m}$)	Commercial filament (Proto-Pasta)	- PLA/CF 15 wt.%	$[0^\circ]/[90^\circ]/[\pm 45^\circ]$ - 53.7/37.0/19.6	$[0^\circ]/[90^\circ]/[\pm 45^\circ]$ - 7.7/4.1/1.3		Decrease in strength and increase in stiffness due to CF.	Ferreira et al. (Ref 33)
PLA	Short carbon fiber ($L = 125 \mu\text{m}$ and $D = 7.4 \mu\text{m}$)	Commercial filament (3DXMax CFR, 3DXTech, USA)	- PLA/CF 15 wt.%	$[0^\circ]/[90^\circ]$ - 53.7-60.6	$[0^\circ]/[90^\circ]$ - 5.7- 6.7		Annealing process improved the mechanical properties.	Ivey et al. (Ref 37)
PLA	Milled carbon fibers ($L = 100 \mu\text{m}$ and $D = 7.2 \mu\text{m}$)	Double extrusion	- PLA - PLA/CF 3 wt.% - PLA/CF 5 wt.% - PLA/CF 7 wt.% - PLA/CF10 wt.%	$[\pm 45^\circ]$ - 48.6 - 50.9 - 54.6 - 48.7 - 49.8				Papon et al. (Ref 31)
PLA	Short carbon fiber ($L = 150\text{-}200 \mu\text{m}$ and $D = 7 \mu\text{m}$)	Commercial filament (Shenzhen Wococo Technology Co., Ltd)	- PLA/CF 20 wt.%	$X[0^\circ]Y[90^\circ]Z$ - 52-54/14-20/36-41				Ding et al. (Ref 30)
PLA	-	Commercial filament (CF-PLA, FFF world S.L., Spain)	- PLA/CF		$[0^\circ]/[90^\circ]/[\pm 45^\circ]$ - 4.4/3.6/3.5			Khudiakova et al. (Ref 38)
PLA	-	Commercial filament (CarbonX™ filament)	- PLA/CF	$X/Y/Z$ - 70.3/66.1/18.2	$X/Y/Z$ - 9.2/8.5/3.4			Reverte et al. (Ref 11)
PLA	Short carbon fibers ($L = 0.1, 0.5, 1$ and 2 mm)	Fiber spraying at interlayers of 3D printing	- PLA - PLA/CF 0.5 wt.% - PLA/CF 1 wt.% - PLA/CF 1.5 wt.% - PLA/CF 2 wt.%	$[0^\circ]$ - 30 - 38 - 35 - 33 - 25	$[0^\circ]$ - 1.2 - 1.8 - 1.1 - 1.2 - 1.2		Optimizing occurred when fiber length of 0.5-1 mm	Fan et al. (Ref 39)

Table 11. continued

Matrix	Reinforcement	Manufacturing technique	Type of fiber reinforcement and amount	Mechanical properties			Detail and comments	Study
				Tensile strength, MPa	Tensile modulus, GPa			
ABS	Milled carbon fiber ($L = 100\text{-}150\ \mu\text{m}$ and $D = 7.2\ \mu\text{m}$)	Mixing in the blender, followed by double extrusion	- ABS - ABS/CF 3 wt.% - ABS/CF 5 wt.% - ABS/CF 7.5 wt.% - ABS/CF 10 wt.% - ABS/CF 15 wt.%	[± 45°] - 34 - 41 - 42 - 41 - 33 - 35	[± 45°] - 2 - 2.1 - 2.5 - 2.5 - 2.2 - 2.3	[± 45°] - Void = 2.5% - Void = 0.5% - Void = 1.0% - Void = 1.5% - Void = 9.0% - Void = 3.3%	Ning et al. (Ref 40)	
ABS	Short carbon fiber ($L = 3.2\ \text{mm}$, after 0.26mm)	Mixing with torque rheometer, followed by extrusion	- ABS - ABS/CF 10 wt.% - ABS/CF 20 wt.% - ABS/CF 30 wt.% - ABS/CF 40 wt.%	[0°] - 31 - 52 - 60 - 62 - 67	[0°] - 2 - 7.5 - 11.5 - 14.0 - 13.8	Highly oriented fibers in the printing direction Void content 16-27%.	Tekinalp et al. (Ref 12)	
ABS	Vapor-grown carbon nanofibers ($L = 100\ \mu\text{m}$ and $D = 0.1\ \mu\text{m}$)	Banbury mixing, followed by screw extrusion	- ABS - ABS/VGCF 10 wt.%	[0°] - 27 - 37	[0°] - 0.49 - 0.79	Good fibers oriented Poor adhesion between fibers and matrix	Shofner et al. (Ref 41)	
ABS	Carbon fiber	Commercial pellets - AS-13CF/000 Black - J-1200/CF/20	- ABS/CF 13 wt.% - ABS/CF 20 wt.%	X/Z - 53.3/17.8 - 66.4/10.3	X/Z - 8.18/2.56 - 11.9/2.1	A high degree of anisotropy	Duty et al. (Ref 35)	
ABS	Carbon fiber	Commercial filament (3DXTech Inc, Michigan, USA)	- ABS - ABS/CF 15 wt.%	[0°]/[90°]/[± 45°] - 27.7/22.3/24.0 - 39.1/13.7/29.2	[0°]/[90°]/[± 45°] - 2.2/1.9/2.1 - 5.9/2.1/2.8	[± 45°] - SS = 12.0 and SM = 0.75 - SS = 14.5 and SM = 0.98	Zhang et al. (Ref 34)	
ABS	Short carbon fiber ($L = 6\ \text{mm}$, after 190-223 μm)	Mixing by twin-screw extrusion, followed by single extrusion	- ABS/CF20 wt.% + SAG 0-7%	[± 45°] - 63.5-73.3 (tensile) and 94-111 (flexural)	[± 45°] - 9-9.4 (flexural)	An increase in void content increase from 10 to 12.5% at 7 wt.% of SAG	Zhu et al. (Ref 42)	
ABS	Short carbon fiber ($L = 10\text{-}278\ \mu\text{m}$, $D = 7.5\ \mu\text{m}$)	Commercial filament (3DXTech Inc, USA)	- ABS/CF 15 wt.%	[0°]/[30°]/[45°]/[60°]/[90°] - 41/25/21/18/15	[0°]/[30°]/[45°]/[60°]/[90°] - 4.1/2.4/2.0/1.9/1.6	[0°] - $G_1 = 0.15\text{-}0.4$	Young et al. (Ref 43)	

Table 11. continued

Matrix	Reinforcement	Manufacturing technique	Type of fiber reinforcement and amount	Mechanical properties			Detail and comments	Study
				Tensile strength, MPa	Tensile modulus, GPa			
ABS	Short carbon fiber ($L = 81 \pm 20 \mu\text{m}$)	Commercial filament (3DXTech Inc, USA)	- ABS - ABS/CF 15 wt.%			[0°] - $G_{IC} = 1.90$ (DCB) and 3.44 (SENB) - $G_{IC} = 0.36$ (DCB) and 3.09 (SENB)	Somireddy et al. (Ref 36)	
PP	Milled carbon fiber ($L = 250 \mu\text{m}$, $D = 7 \mu\text{m}$)	Mixing by compounder, followed by single extrusion	- PP - PP/CF 10 wt.%	[0°]/[90°]/[0°/90°]/ [± 45°] - 31.5/30.1/28.2/29.5 - 74.2/36.5/51.4/44.5	[0°]/[90°]/[0°/90°]/ [± 45°] - 1.14/1.03/0.99/0.99 - 5.60/1.65/3.39/1.92		Spoerk et al. (Ref 13)	
PP	Glass fiber ($D = 11-15 \mu\text{m}$)	Extrusion of commercial pellets	- PP - PP/GF 30 wt.%	[± 45°] - 20 - 34	[± 45°] - 0.06 - 0.39		Sodeifan et al. (Ref 44)	
PEEK	Glass fiber ($L = 196 \mu\text{m}$, $D = 11.7 \mu\text{m}$) Carbon fiber ($L = 205 \mu\text{m}$, $D = 6.5 \mu\text{m}$)	Twin-screw extrusion followed by single-screw extrusion	- PEEK - PEEK/GF 5 wt. % - PEEK/GF 10 wt. % - PEEK/GF 15 wt. % - PEEK/CF 5 wt. % - PEEK/CF 10 wt. % - PEEK/CF 15 wt. %	[± 45°] - 78.8 - 86.0 - 82.8 - 79.1 - 94.0 - 84.7 - 83.4	[± 45°] - IS = 30.2 - IS = 28.0 - IS = 21.2 - IS = 24.9 - IS = 22.0 - IS = 18.3		Wang et al. (Ref 14)	
PEEK	Carbon fiber ($L = 100 \mu\text{m}$)	Twin-screw extrusion with single-screw feeder	- PEEK - PEEK/CF5 wt. %	X/Y - 134/146 (flexural) - 124/146 (flexural)	X/Y - 3.39/3.44 (flexural) - 3.10/3.74 (flexural)	X/Y - Void = 2.60%/ 2.62% - Void = 3.00%/ 4.38%	Qiushi et al. (Ref 26)	
PA	Short carbon fiber ($L = 15-20 \text{mm}$, $D = 6-7 \mu\text{m}$)	Twin-screw extrusion followed by single-screw extrusion	- PA12 - PA12/CF2 wt. % - PA12/CF4 wt. % - PA12/CF6 wt. % - PA12/CF8 wt. % - PA12/CF10 wt. %	[0°] - 47 - 53 - 58 - 79 - 87 - 94	[0°] - 0.95 - 1.45 - 1.95 - 2.80 - 3.35 - 3.60	[0°] - IS = 22.5 - IS = 12.4 - IS = 12.5 - IS = 18.8 - IS = 19.8 - IS = 24.8	Guangxin et al. (Ref 15)	

Table 11. continued

Matrix	Reinforcement	Manufacturing technique	Type of fiber reinforcement and amount	Mechanical properties			Detail and comments	Study
				Tensile strength, MPa	Tensile modulus, GPa			
PA	Short carbon fiber (L = 100 μm)	Commercial filament (Fibreforce, Italy)	- PA/CF6 vol.%	[0°] - 33.5	[0°] - 1.85	[0°] - FS = 55.3 and FM = 3.0	Block et al. (Ref 45)	
PA	Short carbon fiber (L = 64 μm, D = 10 μm)	Commercial filament (3DXTech Inc, Michigan, USA)	- PA/CF 20 wt.%	[0°] - 52	[0°] - 6.19	[0°] - CoS = 56 and CoM = 3.93	Verdejo et al. (Ref 46)	
PA	Short carbon fiber (L = 94 μm, D = 6.5 μm)	Commercial filament (Roboze SpA, Bari, Italy)	- PA/CF 15 wt.%	[0°]/[± 45°] - 105.8/72.9	[0°]/[± 45°] - 11.71/7.73	[0°]/[± 45°] - Void = 11.3%/13.8%	Lupone et al. (Ref 16)	
PA	Short carbon fiber	Extrusion of commercial pellets	- PA - PA/CF 15 wt.%	X[± 45°]/Z[± 45°] - 71.4/26.0 - 95.7/27.8	X [± 45°]/Z[± 45°] - 3.18/2.80 - 7.87/2.90	X [± 45°]/Z[± 45°] - IS = 111/7.7 - IS = 66.1/10.6	This study (2020)	

Data of PLA, ABS, PP, PEEK and PA composites are presented in order
 FS, flexural strength (MPa); FM, flexural modulus (GPa); CoS, compressive strength (MPa); CoM, compressive modulus (GPa); K_{OC} , conditional stress intensity factor (MPa m^{1/2}); K_{QC} , critical stress intensity factor (MPa m^{1/2}); G_Q , conditional strain energy release rate (kJ/m²); G_{IC} , critical strain energy release rate (kJ/m²); IS, impact strength (kJ/m²); ILSS, interlaminar shear strength (MPa); SS, shear strength (MPa); SM, shear modulus (GPa); DCB, double cantilever beam test; SENB, single end notch bend test; SAG, acrylonitrile, and glycidyl methacrylate.

3. Following these findings, PA/CF composite appears as a good candidate to be used for self-sensing material in structural health monitoring purposes, especially at high-temperature applications up to about 120 °C.

Acknowledgment

The authors kindly acknowledge Dr. Thiago Medeiros Araujo (Lehmann & Voss & Co. KG, Hamburg, Germany) for providing the pellets of Luvocom PA and PA/CF composites used in this study.

Funding

Open access funding provided by Università degli Studi di Trento within the CRUI-CARE Agreement.

Open Access This article is licensed under a Creative Commons Attribution 4.0 International License, which permits use, sharing, adaptation, distribution and reproduction in any medium or format, as long as you give appropriate credit to the original author(s) and the source, provide a link to the Creative Commons licence, and indicate if changes were made. The images or other third party material in this article are included in the article's Creative Commons licence, unless indicated otherwise in a credit line to the material. If material is not included in the article's Creative Commons licence and your intended use is not permitted by statutory regulation or exceeds the permitted use, you will need to obtain permission directly from the copyright holder. To view a copy of this licence, visit <http://creativecommons.org/licenses/by/4.0/>.

References

- ASTM F2792-12a, *Standard Terminology for Additive Manufacturing Technologies*, ASTM International, 2012
- O. Mohamed, S. Masood, and J. Bhowmik, Optimization of Fused Deposition Modeling Process Parameters: A Review of Current Research and Future Prospects, *Adv. Manuf.*, 2015, **3**(1), p 42–53
- S. Dul, L. Fambri, and A. Pegoretti, Fused Deposition Modelling with ABS–Graphene Nanocomposites, *Compos. A Appl. Sci. Manuf.*, 2016, **85**, p 181–191
- M.L. Shofner, K. Lozano, F.J. Rodriguez-Macias, and E.V. Barrera, Nanofiber-Reinforced Polymers Prepared by Fused Deposition Modelling, *J. Appl. Polym. Sci.*, 2003, **89**(11), p 3081–3090
- S. Anjum, F. Lars, and I. Azhar, High Performance Thermoplastic Composites: Study on the Mechanical, Thermal, and Electrical Resistivity Properties of Carbon Fiber-Reinforced Polyetheretherketone and Polyethersulphone, *Polym. Compos.*, 2007, **28**(6), p 785–796
- N. van de Werken, H. Tekinalp, P. Khanbolouki, S. Ozcan, A. Williams, and M. Tehrani, Additively Manufactured Carbon Fiber-Reinforced Composites: State of the Art and Perspective, *Addit. Manuf.*, 2020, **31**, p 100962–100980
- J.J. Fallon, S.H. McKnight, and M.J. Bortner, Highly Loaded Fiber Filled Polymers for Material Extrusion: A Review of Current Understanding, *Addit. Manuf.*, 2019, **30**, p 100810–100820
- P. Parandoush and D. Lin, A Review on Additive Manufacturing of Polymer-Fiber Composites, *Compos. Struct.*, 2017, **182**, p 36–53
- X. Wang, M. Jiang, Z. Zhou, J. Gou, and D. Hui, 3D Printing of Polymer Matrix Composites: A Review and Prospective, *Compos. Part B-Eng.*, 2017, **110**, p 442–458
- S. Dul, L. Fambri, and A. Pegoretti, Development of New Nanocomposites for 3D Printing Applications, *Structure and Properties of Additive Manufactured Polymer Components*, 1st ed., K. Friedrich, R.

- Walter, C. Soutis, S.G. Advani, I.H.B. Fiedler Ed., Woodhead Publishing, Sawston, 2020, p 17–59
11. J.M. Reverte, M.Á. Caminero, J.M. Chacón, E. García-Plaza, P.J. Núñez, and J.P. Becar, Mechanical and Geometric Performance of PLA-Based Polymer Composites Processed by the Fused Filament Fabrication Additive Manufacturing Technique, *Materials*, 2020, **13**(8), p 1924–1939
 12. H.L. Tekinalp, V. Kunc, G.M. Velez-Garcia, C.E. Duty, L.J. Love, A.K. Naskar, C.A. Blue, and S. Ozcan, Highly Oriented Carbon Fiber-Polymer Composites via Additive Manufacturing, *Compos. Sci. Technol.*, 2014, **105**, p 144–150
 13. M. Spoerk, C. Savandaiah, F. Arbeiter, G. Traxler, L. Cardon, C. Holzer, and J. Sapkota, Anisotropic Properties of Oriented Short Carbon Fibre Filled Polypropylene Parts Fabricated by Extrusion-Based Additive Manufacturing, *Compos. A Appl. Sci. Manuf.*, 2018, **113**, p 95–104
 14. P. Wang, B. Zou, S. Ding, C. Huang, Z. Shi, Y. Ma, and P. Yao, Preparation of Short CF/GF Reinforced PEEK Composite Filaments and Their Comprehensive Properties Evaluation for FDM-3D Printing, *Compos. B Eng.*, 2020, **198**, p 108175–108186
 15. G. Liao, Z. Li, Y. Cheng, D. Xu, D. Zhu, S. Jiang, J. Guo, X. Chen, G. Xu, and Y. Zhu, Properties of Oriented Carbon Fiber/Polyamide 12 Composite Parts Fabricated by Fused Deposition Modeling, *Mater. Des.*, 2018, **139**(Supplement C), p 283–292
 16. F. Lupone, E. Padovano, A. Veca, L. Franceschetti, and C. Badini, Innovative Processing Route Combining Fused Deposition Modelling and Laser Writing for the Manufacturing of Multifunctional Polyamide/Carbon Fiber Composites, *Mater. Des.*, 2020, **193**, p 108869–108880
 17. A.A. Stepashkin, D.I. Chukov, F.S. Senatov, A.I. Salimon, A.M. Korsunsky, and S.D. Kaloshkin, 3D-Printed PEEK-Carbon Fiber (CF) Composites: Structure and Thermal Properties, *Compos. Sci. Technol.*, 2018, **164**, p 319–326
 18. M.A. Saleh, R. Kempers, and G.W. Melenka, 3D Printed Continuous Wire Polymer Composites Strain Sensors for Structural Health Monitoring, *Smart Mater. Struct.*, 2019, **28**(10), p 105041–105052
 19. ASTM D792 Standard Test Methods for Density and Specific Gravity (Relative Density) of Plastics by Displacement, ASTM International, 2013, p 1-6
 20. R.H. Mehta, Physical Constants of Various Polyamides, *Polymer Handbook*, 4th ed., J. Brandrup, E.H. Immergut, E.A. Grulke Ed., Wiley-Interscience, 1998, p V/126
 21. ASTM D1525 Standard Test Method for Vicat Softening Temperature of Plastics, ASTM International, 2009
 22. ISO 527-1:2012 Plastics—Determination of Tensile Properties—Determination of Tensile Properties—Part 2: Test Conditions for Moulding and Extrusion Plastics (ISO 527-2:2012), 2012
 23. ASTM D790 Standard Test Methods for Flexural Properties of Unreinforced and Reinforced Plastics and Electrical Insulating Materials, ASTM International, 2017
 24. ISO 179-1:2010 Plastics—Determination of Charpy Impact Properties - Part 1: Non-instrumented Impact Test (ISO 179-1:2010), 2011
 25. ASTM 5045 Standard Test Methods for Plane-Strain Fracture Toughness and Strain Energy Release Rate of Plastic Materials, ASTM International, 2014
 26. Q. Li, W. Zhao, Y. Li, W. Yang, and G. Wang, Flexural Properties and Fracture Behavior of CF/PEEK in Orthogonal Building Orientation by FDM: Microstructure and Mechanism, *Polymers*, 2019, **11**(4), p 656
 27. T. Kawaguchi, The Dynamic Mechanical Properties of Nylons, *J. Appl. Polym. Sci.*, 1959, **2**(4), p 56–61
 28. J. Horský, J. Kolařík, and L. Fambri, Gradient Composites of Alkaline Poly(6-hexanelactam) with Graphite: One-Step Synthesis, Structure, and Mechanical Properties, *Macromol. Mater. Eng.*, 2001, **286**(4), p 216–224
 29. J. Pagacz, K.N. Raftopoulos, A. Leszczyńska, and K. Pielichowski, Bio-polyamides based on renewable raw materials, *J. Therm. Anal. Calorim.*, 2016, **123**(2), p 1225–1237
 30. Q. Ding, X. Li, D. Zhang, G. Zhao, and Z. Sun, Anisotropy of Poly(Lactic Acid)/Carbon Fiber Composites Prepared by Fused Deposition Modeling, *J. Appl. Polym. Sci.*, 2020, **137**(23), p 48786–48796
 31. E.A. Papon and A. Haque, Fracture Toughness of Additively Manufactured Carbon Fiber Reinforced Composites, *Addit. Manuf.*, 2019, **26**, p 41–52
 32. S. Dul, A. Pegoretti, and L. Fambri, Fused Filament Fabrication of Piezoresistive Carbon Nanotubes Nanocomposites for Strain Monitoring, *Front. Mater.*, 2020, **7**, p 12
 33. R.T.L. Ferreira, I.C. Amatte, T.A. Dutra, and D. Bürger, Experimental Characterization and Micrography of 3D Printed PLA and PLA Reinforced with Short Carbon Fibers, *Compos. B Eng.*, 2017, **124**, p 88–100
 34. W. Zhang, C. Cotton, J. Sun, D. Heider, B. Gu, B. Sun, and T.-W. Chou, Interfacial Bonding Strength of Short Carbon Fiber/Acrylonitrile-Butadiene-Styrene Composites Fabricated by Fused Deposition Modeling, *Compos. B Eng.*, 2018, **137**, p 51–59
 35. E.C. Duty, V. Kunc, B. Compton, B. Post, D. Erdman, R. Smith, R. Lind, P. Lloyd, and L. Love, Structure and mechanical behavior of Big Area Additive Manufacturing (BAAM) materials, *Rapid Prototyping J.*, 2017, **23**(1), p 181–189
 36. M. Somireddy, C.V. Singh, and A. Czekanski, Mechanical Behaviour of 3D Printed Composite Parts with Short Carbon Fiber Reinforcements, *Eng. Fail. Anal.*, 2020, **107**, p 104232–104244
 37. M. Ivey, G.W. Melenka, J.P. Carey, and C. Ayranci, Characterizing Short-Fiber-Reinforced Composites Produced Using Additive Manufacturing, *Adv. Manuf. Polym. Compos. Sci.*, 2017, **3**(3), p 81–91
 38. A. Khudiakova, F. Arbeiter, M. Spoerk, M. Wolfahrt, D. Godec, and G. Pinter, Inter-Layer Bonding Characterisation Between Materials with Different Degrees of Stiffness Processed by Fused Filament Fabrication, *Additive Manufacturing*, 2019, **28**, p 184–193
 39. C. Fan, Z. Shan, G. Zou, L. Zhan, and D. Yan, Performance of Short Fiber Interlayered Reinforcement Thermoplastic Resin in Additive Manufacturing, *Materials*, 2020, **13**(12), p 2868–2884
 40. F. Ning, W. Cong, J. Qiu, J. Wei, and S. Wang, Additive Manufacturing of Carbon Fiber Reinforced Thermoplastic Composites Using Fused Deposition Modeling, *Compos. B Eng.*, 2015, **80**, p 369–378
 41. M.L. Shofner, F.J. Rodriguez-Macias, R. Vaidyanathan, and E.V. Barrera, Single Wall Nanotube and Vapor Grown Carbon Fiber Reinforced polymers processed by extrusion freeform fabrication, *Compos. Pt. A-Appl. Sci. Manuf.*, 2003, **34**(12), p 1207–1217
 42. J. Zhu, J. Zhang, J. Wang, and B. Wang, Compatibilizer Assisted SCF/ABS Composites with Improved Mechanical Properties Prepared by Fused Deposition Modeling, *Polym.-Plast. Technol. Eng.*, 2018, **57**(15), p 1576–1584
 43. D. Young, N. Wetmore, and M. Czabaj, Interlayer Fracture Toughness of Additively Manufactured Unreinforced and Carbon-Fiber-Reinforced Acrylonitrile Butadiene Styrene, *Additive Manufacturing*, 2018, **22**, p 508–515
 44. G. Sodeifian, S. Ghaseminejad, and A.A. Yousefi, Preparation of Polypropylene/Short Glass Fiber Composite as Fused Deposition Modeling (FDM) Filament, *Results Phys.*, 2019, **12**, p 205–222
 45. L.G. Blok, M.L. Longana, H. Yu, and B.K.S. Woods, An Investigation into 3D Printing of Fibre Reinforced Thermoplastic Composites, *Addit. Manuf.*, 2018, **22**, p 176–186
 46. E. Verdejo de toro, J. Coello Sobrino, A. Martínez Martínez, V. Migueleña, and J. Ayllón Pérez, Investigation of a Short Carbon Fibre-Reinforced Polyamide and Comparison of Two, *Materials*, 2020, **13**(3), p 672–684

Publisher's Note Springer Nature remains neutral with regard to jurisdictional claims in published maps and institutional affiliations.